Reduction of Unsteady Stator Rotor Interaction by Trailing Edge Blowing Using MEMS Based Microvalves

by

Nikhil M. Rao

Thesis submitted to the Faculty of the
Virginia Polytechnic Institute and State University
in partial fulfillment of the requirements for the degree of

Master of Science

in

Mechanical Engineering

Wing F. Ng, Chair
Clint L. Dancey
Ricardo D. Burdisso

April 1999

Blacksburg, Virginia

Key words: Turbomachinery, Noise, Aeroacoustics, Trailing Edge Blowing, MEMS.

Reduction of Unsteady Stator Rotor Interaction by Trailing Edge Blowing Using MEMS Based Microvalves

by

Nikhil M. Rao

Dr. W.F. Ng, Chairman

Mechanical Engineering

(ABSTRACT)

This research performs an experimental study of a trailing edge blowing system that can adapt to variations in flow parameters and reduce the unsteady stator-rotor interaction at all engine operating conditions. The fan rotor of a 1/14 scale turbofan propulsion simulator is subjected to spatially periodic, circumferential inlet flow distortions. The distortions are generated by four struts that support a centerbody in the inlet mounted onto the simulator. To reduce the unsteady effects of the strut wakes on the rotor blades, the wake is re-energized by injecting mass from the trailing edge of the strut. Each strut is provided with discrete blowing holes that open out through the strut trailing edge. Each blowing hole is connected to a MEMS based microvalve, which controls the blowing rate of the hole. The microvalve is actuated by a signal voltage, generated by a PID controller that accepts free stream and wake axial flow velocities as inputs and minimzes their difference. To quantify the effectiveness of trailing edge blowing the far-field noise is measured in an anechoic chamber. The experiments are performed for two simulator test speeds, 29,500 rpm and 40,000 rpm, with and without trailing edge blowing. The maximum reduction recorded at 29,500 rpm is 8.2 dB, and at 40,000 rpm is 7.3 dB. Reductions of 2.9 dB and greater are observed at the first five harmonics of the blade passing frequency. The sound power level at the blade passing frequency, calculated from measured far-field directivity, is reduced by 4.4 dB at 29,500 rpm and by 2.9 dB at 40,000 rpm. The feasibility and advantage of active control is demonstrated by the ability of the system to respond to a step change in the inlet flow velocity, and achieve optimum wake filling in approximately 8 seconds.

Acknowledgments

I would like to thank Dr. Wing Ng for the opportunity to work on this research and for his encouragement and support towards my academic success. I would also like to express my gratitude to committee members, Dr. Ricardo Burdisso and Dr. Clint Dancey for providing me with valuable advice during my research, as also for the excellent instruction I received from them.

I enjoyed every moment of my time here thanks to the team of wonderful people put together by Dr. Ng. I would like to thank Carol Hanuska, Chris Saunders, Yang Fjordingam, Dr. Jon Fleming, and Brooks Moses for their patience while I learnt the nuts and bolts of the research. I would like to thank Jinwei Feng and Jeff Kozak for their effort and assistance towards the research program. I wish both of you the very best in your graduate endeavors. The helpful suggestions and assistance of Tom Leitch and Jon Watts are greatly appreciated. Their unique brand of encouragement was a great help, particularly during the preparation of this document. Special thanks to Bill Stinnett for his “controlled” contribution during the testing and his constant encouragement during the writing of the thesis. Special thanks to Dwight Smith and Todd Bailie for their assistance, advice, encouragement, and editorial experitse. I would like to thank Jeni Kirk, Hank Grabowski, Bill Venner, Lenz Chu, and Greg Ariff for their friendship and for an

enjoyable two years in Blacksburg. To Kirsten and Oliver Popp and Jim Bubb thank you very much for your insight, encouragement, friendship, and support.

Finally to the people who matter most, my family and friends back home. Your faith in me is always a source of motivation. The happiness you derive from my achievements will always inspire me to do my best. You make this effort more meaningful. Thank you very much for your love, patience, and encouragement.

Nikhil M. Rao

Virginia Polytechnic Institute and State University

April 1999.

Table of Contents

List of Illustrations

List of Tables

Nomenclature

a	inlet radius (m)
B	number of rotor blades
BPF	blade passing frequency (Hz)
c	speed of sound (m/sec)
C_s	stator chord length (m)
dB	Decibel, sound pressure level, reference pressure 20×10^{-6} (Pa)
f	frequency (Hz)
$f_{m\mu}$	cut-off frequency (Hz)
k	wave number of standing mode (1/m)
$k_{x\mu}$	axial wave number
$k_{m\mu}$	characteristic number associated with E-functions
N	shaft rotational speed (RPM)
P_t	total pressure (Pa)
p_{rms}	is the rms pressure (Pa)
r	radius (m)
SPL	sound pressure level
V	number of stator vanes
W	sound power (Watts)

Subscripts

k	integer index, wave number of standing mode (1/m)
m	number of lobes or cycles of circumferential pressure variation
n	index, denotes harmonic of BPF

Greek Symbols

β	normalizing factor $(1-M^2)^{1/2}$
μ	radial nodes in the pressure patterns
ν_{nm}	characteristic wave number associated with the E-functions
θ	angular position (rad)
ρ	is density of air (kg/m^3)
σ	hub to tip ratio
Ω_m	Angular velocity of spinning mode of order m (rad/sec)
Ω	Rotor angular velocity (rad/sec)
ω	frequency (rad/sec)
Ψ_z	angle of Zero lobe in radiative directivity (deg)
Ψ_p	angle of Principal lobe in radiative directivity (deg)

Chapter 1

Introduction

Aircraft noise as a source of noise pollution has a significant impact on the environment. Ground based perception of engine noise depends to a large extent on the position of the aircraft in relation to its observer. In-flight noise is perceived as a broadband roar, while at approach and take-off the high pitch rotor noise contributes significantly to the radiated acoustic field. According to Trefny and Wasserbauer (1986), “the forward-propagated fan noise is a significant component during takeoff and approach”. Tyler and Sofrin (1962) noted that, “the discrete frequency compressor whine is more objectionable than broadband exhaust noise”. Airport communities bear the full brunt of this discrete frequency noise. Commonly reported effects of this are eroded property values, social problems inducing stress, health hazards, and reduced tax base affecting schools. This has led to the formulation of many restrictions by government agencies and airport management. Measures like regulating flight paths, curfews on aircraft operations, categories of aircraft that can utilize airport, are designed to reduce exposure levels to people in the airport neighborhood. This has a direct impact on the economy of airports, airlines, and manufacturers, and also affects commerce by restricting free movement of personnel and commodities.

With the evolution of the turbofan engine, the problem of fan noise increased considerably. The trend of aircraft engine noise has been the growing dominance of turbofan noise in the

radiated acoustic field. Particularly during high thrust operations, such as take-off, reported sound levels radiated by turbofans are typically 15 – 20 dB greater than the broadband noise. Furthermore, with higher bypass ratio engines being the norm, the noise levels can only be expected to rise.

Generation of fan noise depends on many factors. Specifically, the discrete frequency radiation is a result of the rotor speed, blade number, and the homogeneity of the flow field. Interaction of the rotor with wakes from upstream obstructions is a major contributor to the far-field noise levels. Previous research by Leitch (1997) on an experimental inlet demonstrated the effectiveness of trailing edge blowing in decreasing the discrete frequency sound levels radiated by a high-speed turbofan simulator on which an inlet with four support struts was mounted. The struts modified the flow field ingested by the rotor by introducing circumferential variations in axial velocity. These wakes increase the radiated far-field sound pressure level at the blade passing frequency and its harmonics.

Prior research on trailing edge blowing experimented with “hard-wired” blowing configurations. Each strut had a certain number of holes, all supplied by a single plenum drilled into the strut. The desired radial variation in blowing rate was obtained by tailoring the blowing hole diameter along the strut span. To achieve this, various configurations were experimentally evaluated, and it was necessary to know the radial variation of axial flow velocity in the wake. The current research investigates a flexible configuration for trailing edge blowing. This scheme provides two distinctive advantages. Global

parameters, such as maximum flow rate necessary, and that possible from geometrical considerations govern the blowing configuration design. To a lesser extent it avoids the need for detailed flow mapping at different global conditions. In the present experiment the trailing edge blowing is accomplished using holes of the same diameter. To account for radial variations in the flow field the system is built “smart”, by incorporating active control and flow control devices. The potential this research has in developing into actual engine application was a driving criterion in the selection of flow control devices. MEMS based microvalves are used for flow control in this research. The small size and weight of these valves make them attractive for engine applications. A significant advantage of incorporating active control is the ability of the system to sense and respond to global changes, such as change in operating conditions. In the context of real engine application such a system is robust, and adaptive. The objectives of this research are to assess the aerodynamic and acoustic benefits derived from the use of active control and MEMS based microvalves.

The experiments are conducted utilizing the experimental inlet used by Leitch (1997). Some modifications, as described in Chapter 3, were made in order to accommodate components of the new system. Blowing rate of each hole is controlled using MEMS based microvalves. Inputting a signal voltage controls the flow rate through these valves. Active control of the microvalves is achieved using a PID feedback controller developed by Feng (1998). The controller minimizes the axial velocity deficit between the wake and the free stream by changing the flow rate through the microvalves. In the current setup the

axial flow velocity in the inlet is radially uniform. This allows the use of a single error sensor for each strut, with a reference signal obtained from a free stream sensor. The effect on wake filling and on the discrete frequency noise radiation is determined through tests in a continuous wind tunnel and an anechoic chamber, respectively. The acoustic testing is done using a 1/14 scale model of a Turbofan Propulsion Simulator, which is representative of modern high bypass ratio engines, as the acoustic source.

This thesis is organized in five chapters. Chapter 2 reviews fan noise, its generation and propagation, noise reduction methods, and previous research. Chapter 3 describes the experimental facilities, setup, hardware and instrumentation used. Chapter 4 presents and discusses the experimental results. Conclusions drawn thereof conclude this thesis in Chapter 5.

Chapter 2

Background

Aircraft noise levels have undergone dramatic changes with the development of engine technology. With the evolution of jet engines aircraft engine noise changed from noise due to piston engines, to jet exhaust noise. According to Greatrex and Bridge (1967), jet noise predominated in the rearward arc of the engine, and the tones due to turbine blade passing were lower than the jet noise. Sir James H. Lighthill (1952) showed that jet noise is of quadrupole origin and varies with the eighth power of jet velocity. With the introduction of bypass turbofan engines it was possible to achieve the same thrust from higher mass flow rates at lower jet velocity. This allowed reduction of the jet noise, to conform to the existing standards, without the added penalty on efficiency incurred by liners and mufflers. As the bypass ratio increased the component of jet noise in total noise reduced, further unmasking the discrete frequency rotor noise. At bypass ratio greater than six, jet noise is irrelevant according to Greatrex & Bridge (1967). With the future in aircraft engines pointing towards higher bypass ratio it is reasonable to assume that unattenuated rotor noise levels will not decrease.

This chapter introduces the theory of fan noise with an emphasis on discrete frequency noise in Section 1. Section 2 will discuss some noise reduction methods. In Section 3 a brief explanation of trailing edge blowing, and previous research in trailing edge blowing is

presented. Finally a section on previous research and the Virginia Tech Aeroacoustic Research Program will conclude this chapter.

2.1 Fan Noise Theory

An acoustic spectrum of the turbofan simulator used at Virginia Tech for acoustic research is shown in Figure (2.1). The notable features of this spectrum are the broadband noise, peak at the blade passing frequency, and the multiple pure tones. In this section these components are discussed briefly. Further discussion is restricted to the problem of discrete frequency radiation, this being the focus of the current research.

2.1.1 Fan Noise - Components

Broadband noise is acoustic energy distributed over a wide range of frequencies. Typically, random aerodynamic processes in the flow generate broadband noise. These processes, characteristically, do not persist over a significant length of time to interact with the rotor repeatedly. Goldstein points out that if the variations are not periodic about a mean value, they tend to produce broadband noise. While independent of the rotor speed, broadband noise does depend on the operating point of the fan. Some of the sources attributed to broadband noise are turbulence in boundary layer flows over rotor blades, stators, and shroud, ingested atmospheric turbulence, and vortex shedding. Washburn and Lauchle (1988) note that broadband noise tends to dominate the spectrum

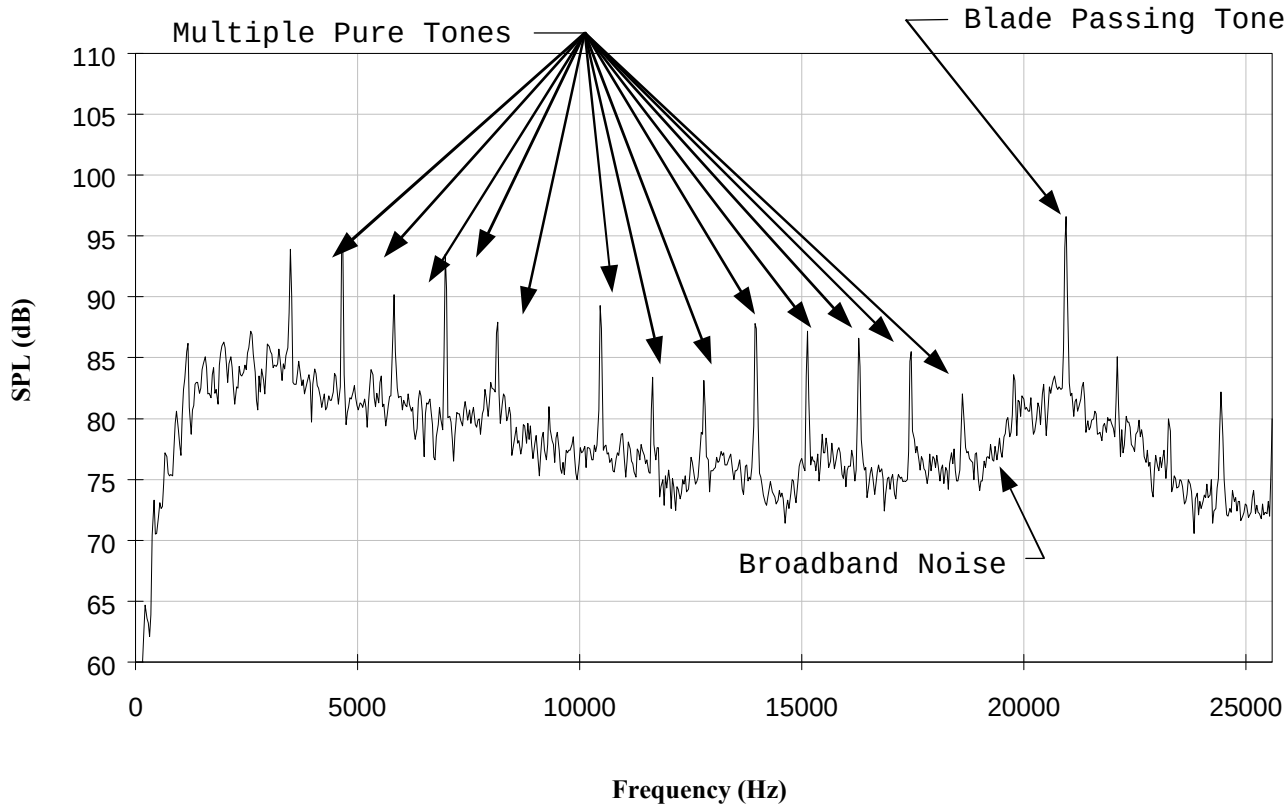

Figure 2.1. Typical Spectrum of the Research Turbofan Simulator

at low flow coefficients, that is when the stage is heavily loaded and is very near to or in stall.

Spectral peaks at the **Blade Passing Frequency** (**BPF**) and its harmonics are functions of the rotor speed and the number of rotor blades. The fluid dynamic sources attributed to discrete frequency radiation are steady blade loading, rotor-stator interaction, stator-rotor interaction, and periodic interaction of the rotor with inlet distortions. According to Roger (1994), "the steady loading noise is a very efficient mechanism for subsonic rotors only if the flow is nearly homogeneous". For sound to be generated at the **BPF** due to interaction with the rotor, the flow must be periodic. In the case of discrete frequency noise due to inlet distortions or turbulence, the length scale of the disturbance should be large enough to interact with a number of rotor blades. The radiated noise also depends on the inlet geometry, and the operating point among other factors. The noise level at the fundamental frequency is usually the loudest, however depending on the energy distribution in the loading harmonics the noise level at any of the harmonics could be a maximum. The sound pressure level at the BPF is typically referred to as the **B**lade **P**assing **T**one (**BPT**), or simply the **Tone**.

Multiple pure tones are seen only when the rotor tip speeds are transonic. They are caused by the presence of standing shockwaves at the leading edge of the rotor blade. Due to manufacturing discrepancies, no two blades are identical, which leads to the presence of multiple peaks. However, all peaks occur at multiples of shaft rotation frequency. Kurosaka (1971) noted that the effect of blade stagger is more important than that of

blade spacing, since blade stagger controls the shock strength, on which depends the amplitude of the acoustic wave.

2.1.2 Discrete Frequency Noise Generation

Flow in turbomachine blade passages behaves like an acoustic dipole. An acoustic dipole consists of two simple sources that are separated by a small distance and vibrate out of phase with each other. Thus as one source compresses the fluid around its boundary, the other source causes an expansion. So while there is no net mass flux in the region, alternating forces setup at the boundaries radiate acoustic waves. Similarly, flow in blade passages is subjected to forces at the solid boundaries. At a particular point in the plane of rotation these forces occur every time a blade passes. Tyler & Sofrin (1962) proved the existence of a pressure pulse associated with each blade. They also proved that this pressure pattern would rotate with an angular velocity equal to that of the rotor. Since the sound is generated due to the periodic interaction of the blades as they rotate in the mean flow, the frequency of the radiated waves is proportional to the rotor speed times the blade number. This is expressed in equation (2.1).

$$BPF\ (\text{Hz}) = \frac{nBN}{60} \qquad \textbf{(2.1)}$$

where; n is any integer, n = 1,2,3,…..

B is the number of rotor blades

N is the shaft speed in rpm

BPF is the Blade Passing Frequency in Hz

An isolated rotor, whether in free space, as in a helicopter, or ducted, as in a turbofan, will generate sound because of the steady aerodynamic loading. Steady loading is characterized by the lift force and is a measure of global energy transferred to the flow. At the blade surface the force is not steady, rather it varies about a mean value. These variations, while very small from the aerodynamic viewpoint, are sufficient to radiate significant amounts of acoustic energy. When the flow is not homogenous, the unsteady loading of the rotor blade is a significant contributor to the radiated sound levels. The unsteady loading is due to rotor interaction with potential and viscous effects of adjacent blade rows and other rotor blades, and inlet distortions. According to Goldstein, the potential effects of adjacent blades decay exponentially away from the obstruction if the mean flow is subsonic. Generally in subsonic mean flow a stage separation of $0.5C_s$, where C_s is stator chord, is considered large enough for these effects to be neglected.

Interaction noise in ducted rotors can be distinguished into rotor noise and stator noise. Rotor noise is due to the periodic interaction of rotor blades with viscous wakes of upstream objects such as struts and inlet guide vanes. As the rotor blades chop through these wakes they experience varying incidence angles and or flow velocities. This causes the lift force to fluctuate about a mean value and hence acoustic waves are radiated into the far-field. In theory, this interaction can produce infinite number of circumferential spinning modes. The number of pressure pulses or peaks a mode generates as it spins in the duct characterize a circumferential mode. However, the only mode shapes that can exist in the duct are given by Equation (2.2). This is because as pointed out by Blake, the

rotor disk acts as a circumferential spatial filter in which samples of wake harmonics from upstream components are made by downstream blading, at integer multiples of the downstream blade number. Another interesting feature of discrete frequency noise as stated by Goldstein is, “Sound radiated at a given frequency by a rotor depends upon all angular harmonics of the wake velocity field, and any given harmonic of the wake contributes to all harmonics of the sound field”.

$$|m| = nB + kV \qquad (2.2)$$

where: m is an integer which gives the number of circumferential peaks in a given spinning mode

n is an integer which indexes the harmonics of the BPF with values from 1 (Fundamental or BPF), 2 (1 Harmonic), 3…

B is number of rotor blades

k is an integer which indexes the harmonics of the upstream disturbance with values …..,-2,-1,0,1,2,…..

V is number of stator vanes

Furthermore, to generate noise at a particular harmonic of the BPF, each spinning mode must rotate with an angular velocity as given by Equation (2.3). As shown later, an important condition for a generated mode to transmit up an inlet is that its angular velocity must be greater than the angular velocity of the rotor.

$$\Omega_m = \frac{nB}{m}\Omega_R \qquad \textbf{(2.3)}$$

where; Ω_m is the angular velocity of the spinning mode in rad/sec

Ω_R is the angular velocity of the rotor in rad/sec

and all other definitions apply as in Equation (2.2)

Stator noise is due to periodic passage of rotor wakes over downstream stators. This causes unsteady lift in the stators, which radiate acoustic energy. Stator noise occurs at the BPF, since it is depends on the blade number and rotor speed. Importantly, the noise at a particular harmonic is caused by the corresponding harmonic of oncoming disturbance.

2.1.3 Transmission

The presence of the duct in turbofan engines modifies not only the flow field but also the acoustic field. Aerodynamically the flow field is more streamlined, causing ingested distortions to stretch and add to discrete frequency noise. Acoustically the duct behaves as a waveguide by reflecting all incident waves. Reflections from the duct wall and the stators cause the acoustic field to be very different from that of free field rotors. Most importantly, the duct geometry dictates the mode shapes that can be present in the duct and propagate the length to radiate into the far – field. This is governed by the axial wave number, k_{xm}, as given by Equation (2.4).

$$k_{xm} = \sqrt{k^2 - k_{mm}^{\ 2}}$$
$$k_{xm} = \frac{2p}{c}\sqrt{f^2 - f_{mm}^{\ 2}} \qquad (2.4)$$

where: c is the speed of sound in m/sec

k is the wave number in 1/m

$k_{m\mu}$ is a characteristic number associated with the E-functions depending upon hub to tip ratio (σ), number of circumferential lobes (m), and the number of nodes or points of zero pressure across the annulus (μ).

f is the frequency of the standing wave pattern in rad/sec

$f_{m\mu}$ is the cutoff frequency of the given mode in rad/sec

Two numbers define each mode shape; m and μ. These respectively describe the number of circumferential lobes in the spinning mode and the number of zeros present across the duct cross section. For a particular mode (m,μ) to propagate down the axis of the inlet, it must have a real axial wave number. For this condition to be satisfied the frequency of the generated acoustic wave must be greater than the cut–off frequency, and then the mode is said to be cut–on. If the axial wave number is imaginary i.e., frequency of the mode is less than the cut–off frequency, then the wave decays exponentially as it propagates down the axis and does not contribute to the far field radiation. These waves are called **evanescent waves**.

The cut-off frequency is determined from E-functions, which are linear combinations of Bessel functions of the first and second kind, that emerge from the solution of the acoustic wave equation in cylindrical coordinates. They depend on the radial pressure distribution, hub to tip ratio of the inlet, the number of circumferential lobes, and the number of nodes or zero pressure points across the annulus.

2.1.4 Far Field Radiation

The radiation of sound from the mouth of the inlet into the far – field is a complicated process, due to diffraction effects at the edge of the inlet. Some of the simple theories proposed neglect the effect of diffraction by assuming an infinitely rigid baffle. According to Homicz and Lordi (1975), while these methods are adequate for predicting directivity in the forward hemisphere, they do not agree with experimental results for sideline radiation, and along the outside of the inlet towards the rear. They further showed that adequate prediction of sideline radiation can be made using a simple unbaffled model. The equations presented by Homicz and Lordi to calculate the angle of the principal lobe and zeros are as given in Equations (2.5). Other researchers have ascertained experimentally the validity of these equations for rotors with hub – tip ratio less than 0.5. As can be seen in the Figure (2.2), from Homicz and Lordi (1975), as the frequency increases well above cut–off, the principal lobe angle shifts towards the axis of the inlet. Also more, narrower lobes are evident. Homicz and Lordi (1975) also note that the only mode that has the peak of its far field pressure on the axis of the inlet is the plane wave mode (m = 0 mode). This mode is also called the symmetric mode. All other modes have a pressure of zero at this position.

$$\mathrm{Cos}\,\Psi_p = \beta\left\{\frac{1-\left(\frac{\nu_{nj}}{\bar{k}\,a}\right)^2}{1-M^2\left[1-\left(\frac{\nu_{nj}}{\bar{k}\,a}\right)^2\right]}\right\}^{1/2} \qquad (2.5)$$

$$\mathrm{Cos}\,\Psi_z = \beta\left\{\frac{1-\left(\frac{\nu_{nj}}{\bar{k}\,a}\right)^2}{1-M^2\left[1-\left(\frac{\nu_{nj}}{\bar{k}\,a}\right)^2\right]}\right\}^{1/2} \quad , \; j \neq m$$

Where :

Ψ_p is the Principal Lobe angle

Ψ_z is the Zero Lobe angle

ν_{nm} characteristic wave number associated with the E-functions

$\beta = (1-M^2)^{1/2}$ is a normalizing factor

$\bar{k} = k / \beta$ is the normalized wave number

a is the inlet radius

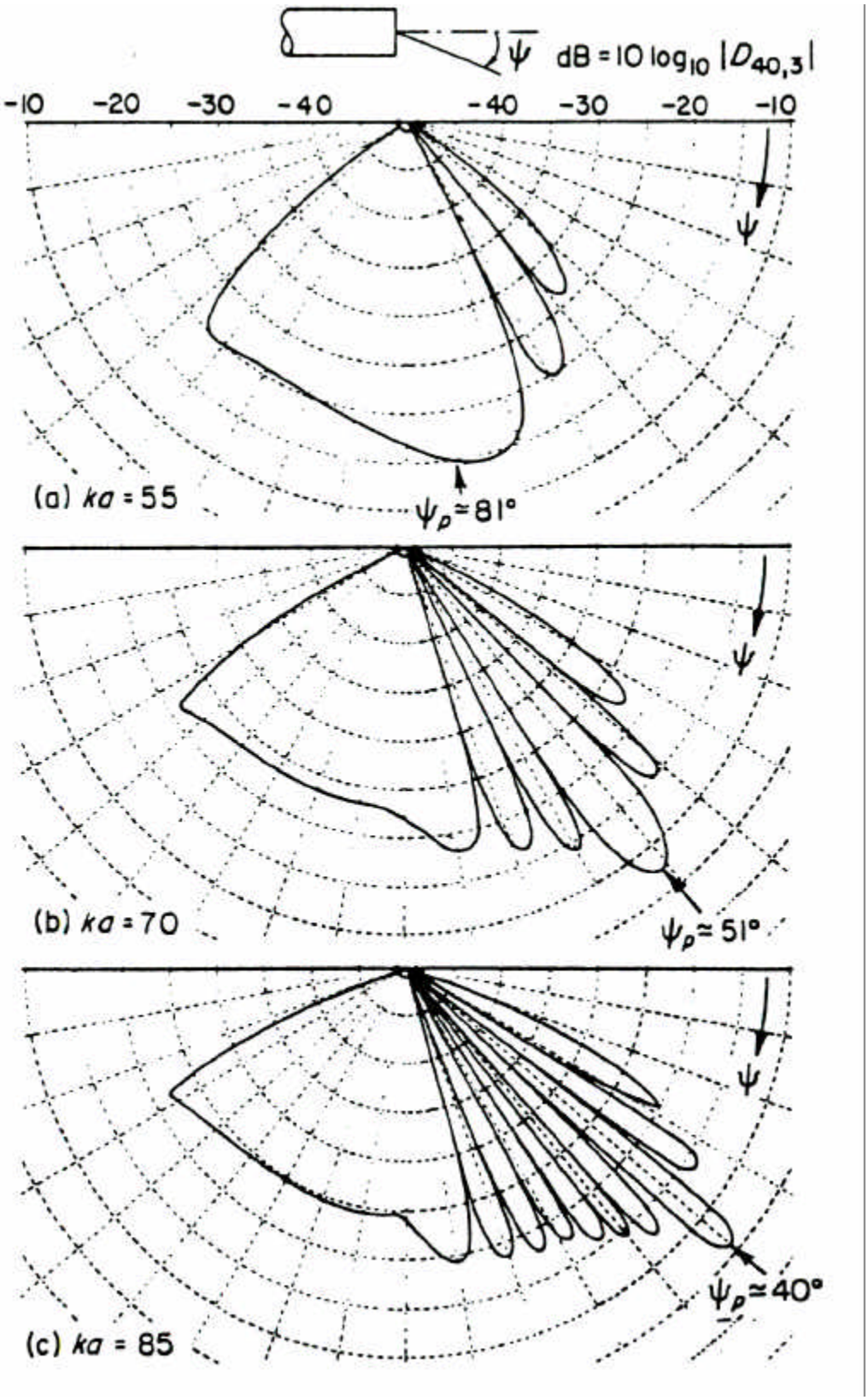

Figure 2.2. Effect of Frequency on Directivity

2.2 Noise Control Methods

Various methods have been developed to reduce the generation and propagation of turbofan noise. The techniques can be broadly classified as passive and active methods. Passive control involves reducing the radiated noise by energy absorption, while the active method involves reducing source strength or modifying acoustic field in the duct to obtain noise reduction. This section briefly describes some of the currently employed solutions to the problem of fan noise.

Probably the most common passive method of noise control is the use of acoustic liners. The liners absorb the radiated acoustic energy, thereby reducing the far–field noise levels. However use of liners increases the engine weight, which is undesirable. Also future developments will see increase in by–pass ratio, while the inlet length is not scaled with diameter. This will make liners less effective.

Among active strategies used or being researched currently are :

i. Introduce anti noise into the duct. Destructive interference leads to reduction of the radiated acoustic power.
ii. Choose the number of rotor blades and stator vanes such that all modes generated at the BPF are cut–off.
iii. Since noise levels typically scale to the sixth power of a characteristic velocity, reducing rotor speed will yield acoustic benefits.
iv. Increased spacing between adjacent blade rows reduces the amplitude of the loading harmonics, which inturn reduces the far-field sound levels.

v. Trailing edge blowing, to fill in the wake and reduce the amplitude of the loading harmonics.

2.3 Trailing Edge Blowing

If a body is placed in the flow of a fluid it causes a low velocity region of flow immediately behind the obstruction. This region is known as the **wake**, and is caused by viscous effects of flow over solid boundaries. Trailing edge blowing is a wake management strategy that employs mass injection off the trailing edge of the body to reduce this velocity defect. As seen in Figure (2.3), the velocity defect and the velocity gradient in the flow are reduced after trailing edge blowing. A sharper wake, as in the baseline case, contains more loading harmonics that contribute to the far-field noise levels. After trailing edge blowing the number of loading harmonics and the amplitude of unsteady loading are reduced. This decreases the far-field noise, since the amplitude of fluctuation of the lift force is reduced. Trailing edge blowing is applicable to rotors as well as stators, and has wide application in the gas turbine engine. It can be used to reduce the noise generated by the initial compressor stages and fan rotor. It can also be employed to reduce other effects of unsteady flow, such as high cycle fatigue, in turbofan and compressor blades.

Leitch (1997) and Saunders (1998) demonstrated experimentally the effectiveness of trailing edge blowing in reducing far-field noise levels, they reported maximum reductions of 7 dB and 6 dB, respectively. Leitch used a generic inlet with four struts.

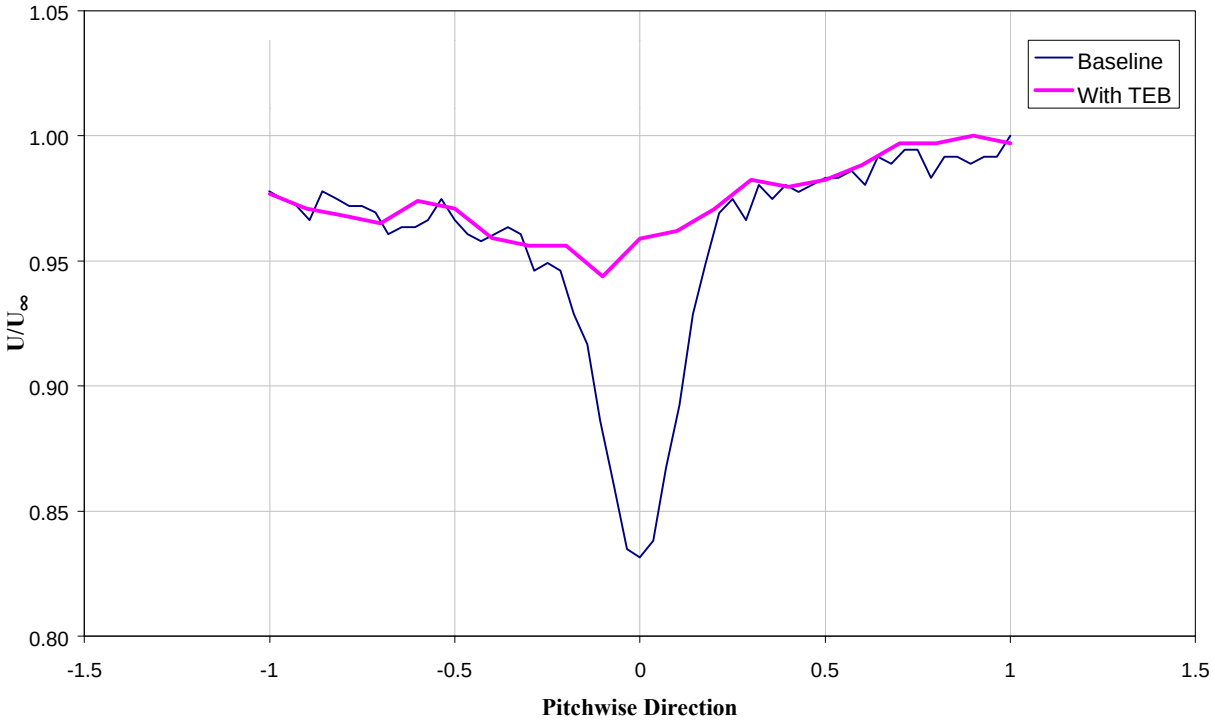

Figure 2.3 Wake Comparison With and Without Trailing Edge Blowing

The struts had flat faces and a blunt trailing edge. Saunders conducted his experiments with an axisymmetric supersonic inlet, with six struts. The struts were airfoil shaped and had a sharp trailing edge. In both cases, extensive bench tests were conducted to tailor the blowing rate of each hole to achieve uniform wake filling at the radial location of the hole. Typically the holes closer to the hub were smaller. The effectiveness of these configurations was highly dependent upon mean flow Mach number, radial variation in Mach number, and the blowing pressure. These configurations are unable to operate optimally at a single, constant source pressure. In the present research the use of MEMS based microvalves and active control allows flexibility in the design of the blowing scheme. The source pressure can be maintained constant over the entire range of operation. This is desirable, since in real engine application, the blowing air would be bled off from a later compressor stage. The ability to respond to radial variations and free stream changes ensures effective operation over a wide range of conditions.

2.4 Previous Research

Throughout this chapter important research has been cited in laying the foundation for this work. This section will note some of the other work done to address the turbomachine noise problem and the research conducted at Virginia Tech.

Waitz, et al., (1995) used numerical and experimental methods to investigate the effect of wake modification on the acoustic radiation from a rotor. They employed trailing edge blowing and boundary layer suction to a rotor blade, to minimize the wake. Estimates of

the radiated noise levels were obtained by a two-dimensional, linearized panel method, LINSUB. Predictions based on experimental aerodynamic data suggested reductions greater than 10 dB in the dominant tones. Waitz, et al. (1995) concluded that wake management is feasible for high-bypass turbofan engines. Also, that trailing edge blowing is more effective than boundary layer suction. Other research by Park and Cimbala (1991), Corcoran (1992), and Naumann (1992) report significant reduction in time-mean wake deficits downstream of a flat plate. Several blowing techniques and configurations were experimented by Corcoran (1992) and Naumann (1992). Corcoran (1992) reports reductions in Reynolds stress and vorticity one chord length downstream. Naumann (1992) experimented various blowing configurations, a continuous slit and a set of discrete jets, with and without vortex generators. This work showed that the most effective method of trailing edge blowing was to use a set of discrete jets, and that the presence of vortex generators enhanced the mixing of the wake with the jets.

2.1.5 Virginia Tech AeroAcoustic Research Program

A large body of research conducted deals with reducing rotor noise and rotor-stator interaction noise. The Virginia Tech Aeroacoustics Program was established in 1991 to investigate the effect of upstream obstructions on rotor noise, i.e. stator-rotor interaction, and explore attenuation possibilities. Most of the research is tailored towards turbofan noise problem in supersonic inlets as the program was established to evaluate the acoustic behavior of inlet designs for the High Speed Civil Transport (HSCT). Several inlet designs

have been tested and attenuation strategies explored. Pande and Ng (1994) evaluated the effect of axial spacing of struts from fanface, on the acoustic radiation. They concluded that increased spacing reduced the interaction noise. Research at Virginia Tech on trailing edge blowing as a means of reducing the radiated noise levels was first conducted by Leitch (1997). Subsequently Saunders (1998) employed trailing edge blowing on an axisymmetric supersonic inlet. Research into effect of “soft choking” on the forward propagated noise has been documented by Detwiler (1993), Hanuska (1998).

Chapter 3

The Experiment

This chapter is divided into three sections. Section 1 describes the test setup for the acoustic testing and the important design considerations involved. Section 2 gives an overview of the test facility and instrumentation. Section 3 details the test matrix and the governing parameters. While this chapter concentrates primarily on the acoustic testing, aerodynamic testing was conducted in a bench test setup to assess the effect of spanwise control. The bench test equipment and test procedure are described in Appendix (A).

3.1 Test Setup

This section illustrates the hardware used for the acoustic testing. It also explains the design of the components involved. Figure (3.1) illustrates the assembled inlet used for this research. The various parts identified are explained in this section. The assembled inlet is mounted onto the Turbofan Propulsion Simulator.

3.1.1 Turbofan Propulsion Simulator

The most important component in this system is the Turbofan Propulsion Simulator (Model 460) from Tech Development Inc. This simulator is modeled on modern, high bypass ratio, turbofan engines, and serves as acoustic source. Figure (3.2) is a picture of the simulator, and it's rotating components. The simulator has a single stage axial fan driven by a single stage axial flow turbine. The fan measures 4.1" in diameter and has 18

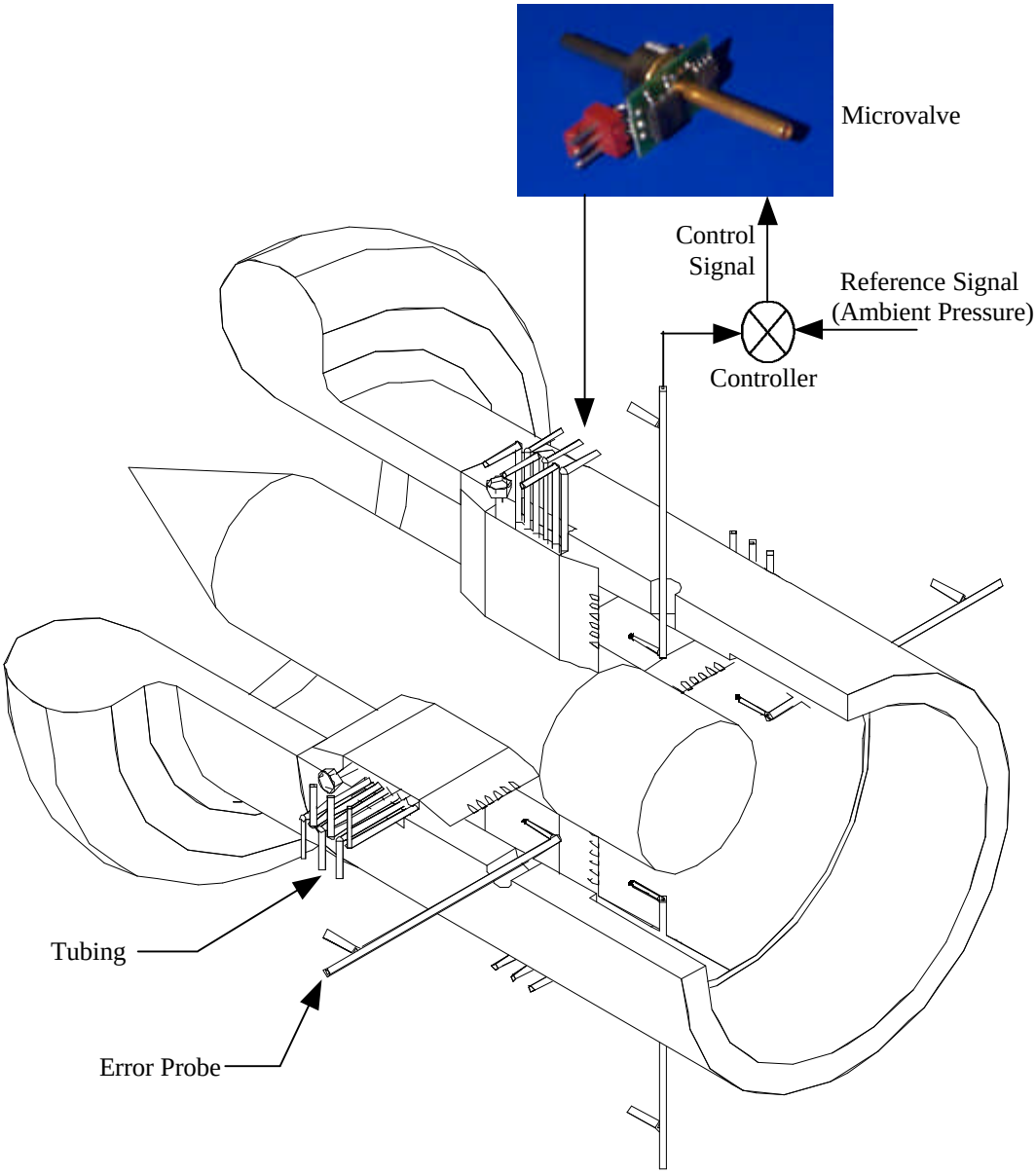

Figure 3.1. Test Setup & Approach

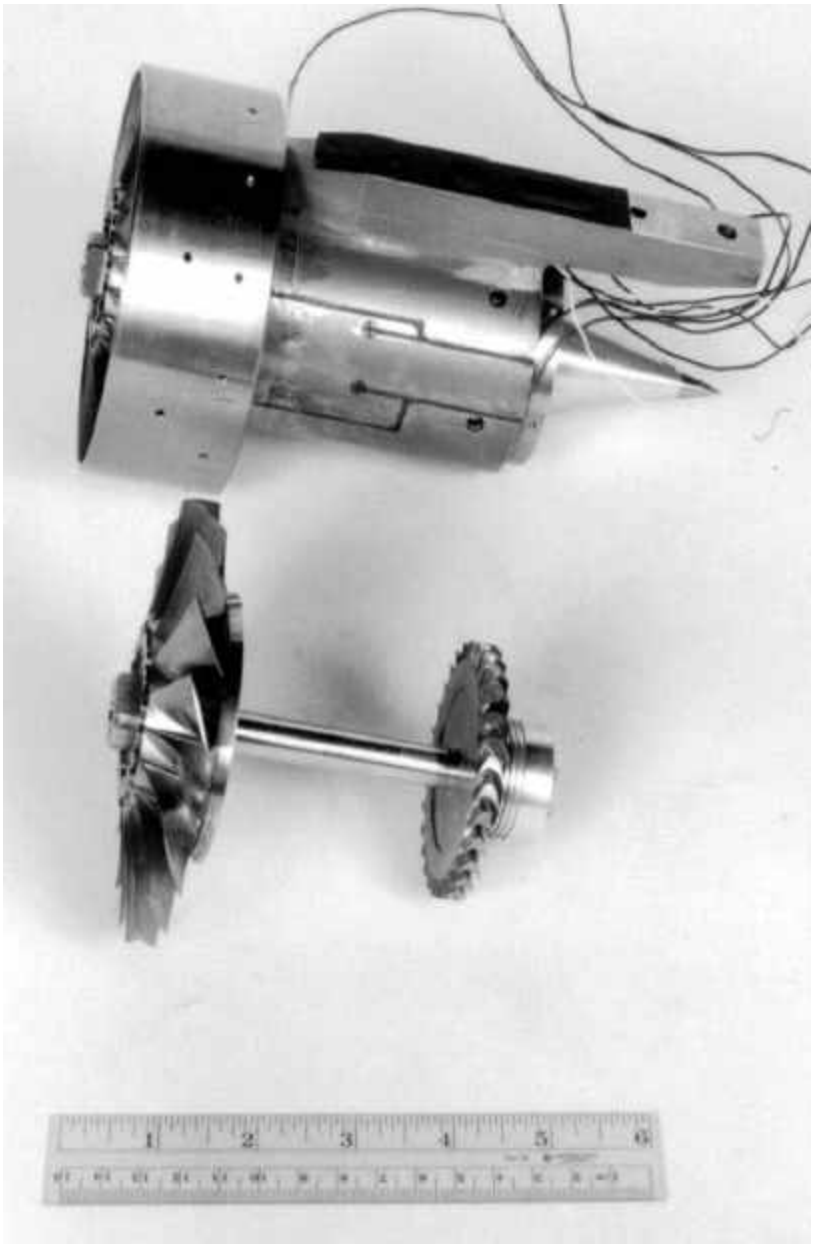

Figure 3.2 Turbofan Propulsion Simulator

blades. It is capable of developing a maximum pressure ratio of 1.6, at a mass flow of 2.72 lbm/sec, (1.23 kg/sec), and maximum speed of 80,000 rpm (100 PNC). A row of 26 Exit Guide Vanes (EGV's) is present one rotor chord length downstream of the fan. These guide vanes also cause far-field noise radiation due to the unsteady lift generated by the passage of rotor wakes. The stage spacing, along with the low test speeds, ensure that the potential effect of the EGV's does not contribute to the unsteady loading of the fan and hence to the acoustic signature of the rotor. The power turbine is a single impulse stage with 29 blades. It is driven by high-pressure air, and can handle a maximum mass flow of 1.50 lbm/sec, (0.68 kg/sec). Figure (3.3) shows the performance curves for the fan and turbine stages. A magnetic speed pickup mounted in the turbine exhaust cone measures the shaft rotational speed. Thermocouples are provided to monitor the bearing temperatures. Accelerometers mounted on the test stand and inlet to monitor vibration levels. All systems have built in redundancy.

3.1.2 Experimental Inlet

Many different inlet configurations were available due to the research carried out under the Virginia Tech Aeroacoustic Program. Trailing edge blowing was employed on two configurations. Leitch (1997) used the symmetric Virginia Tech Experimental Inlet (VTEI) with four struts, while Saunders (1998) used the axisymmetric supersonic inlet with six struts. It was clear at the outset that the system would be very elaborate, and hence to minimize the complexity, the VTEI was chosen to conduct this research. Figure (3.4) shows the inlet with centerbody and support struts. This inlet is neither a

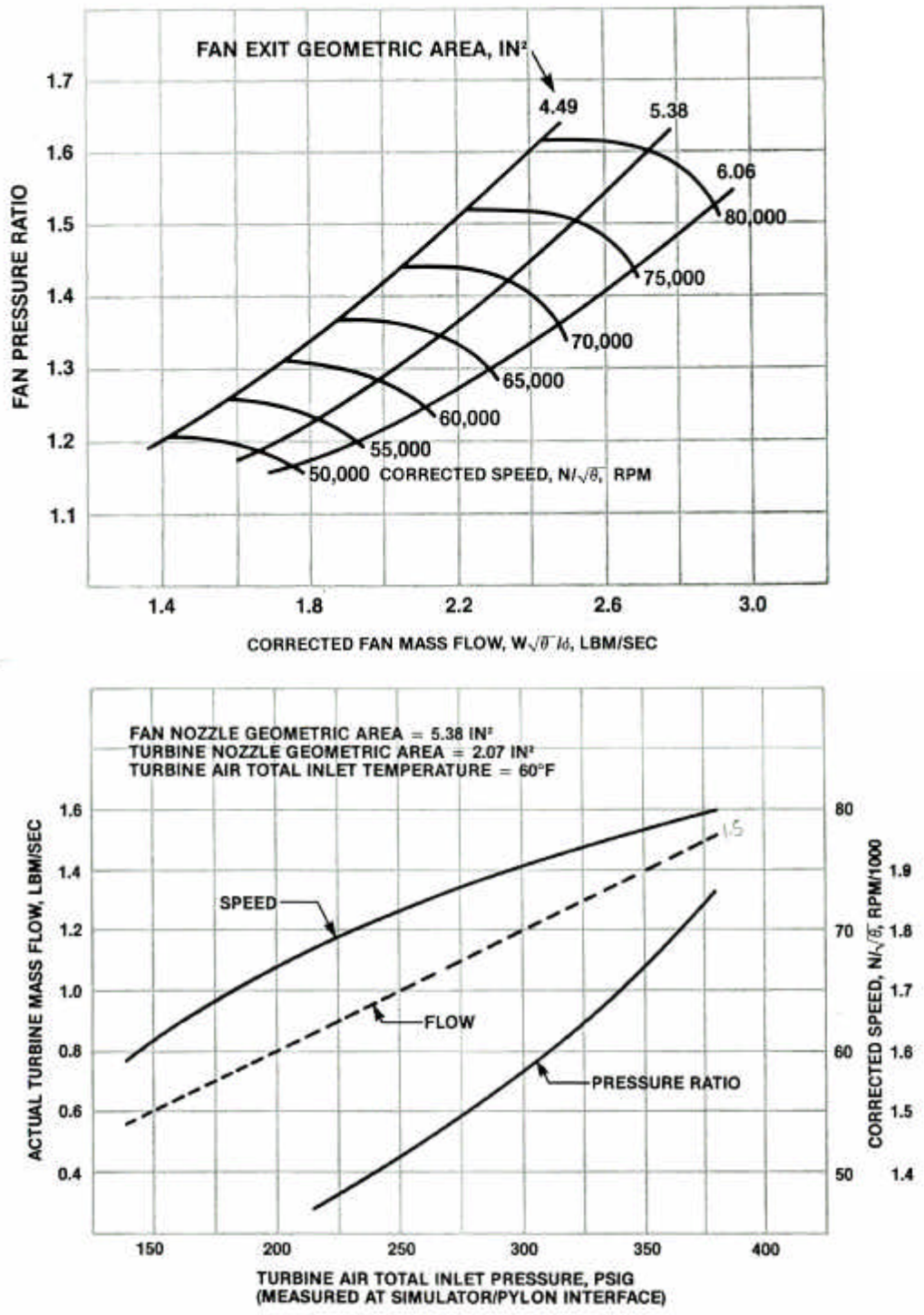

Figure 3.3 TPS Fan and Turbine Performance Maps

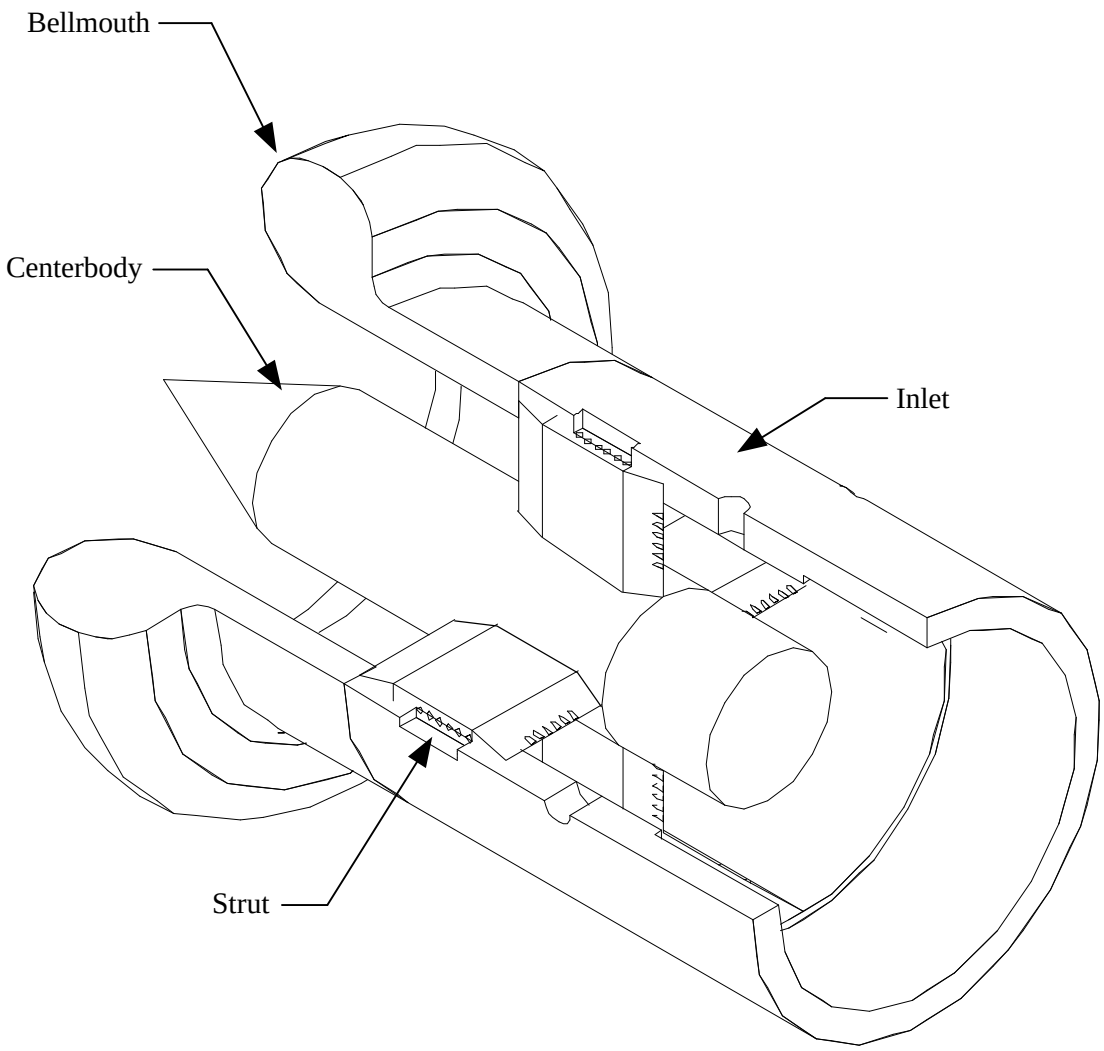

Figure 3.4. Section View of Experimental Inlet

conventional subsonic inlet nor is it a true supersonic inlet. As the comparison in Figure (3.5) shows this inlet is longer than a Conventional Take Off & Landing (CTOL) inlet but shorter than a supersonic inlet. Since the purpose of the experiment is to study the effect of periodic upstream disturbances on rotor noise, the inlet has four struts that support the centerbody. The inlet is a constant area duct with a diameter of 4.1". A larger diameter step at the discharge end allows the inlet to be mounted on the simulator. The mouth of the inlet is provided with a bellmouth to avoid inlet flow separation. Five tapped holes (NPT 1/8") are provided circumferentially. The centers of four of these line up with the trailing edge of each strut, and the remaining one is positioned in the free stream. These holes are used for mounting the flow sensors. The centerbody is a cylinder with a conical section at the inlet. This allows for smooth turning of the flow entering the inlet. The annulus area between the centerbody and inside diameter of the inlet is of constant cross section. Four slots are cut on the surface of the centerbody, 90^{o} apart. The struts are placed in these slots and hence a smooth geometric transition is obtained. Upon assembly, care is taken to fill in all cavities, to avoid the interaction of the rotor with flow distortions generated by these.

3.1.3 Strut

The four support struts serve as the wake generators. They introduce spatially periodic distortions in the flow field ingested by the rotor. The struts are faceted, with sharp leading and trailing edges and provide no turning to the flow. Figure (3.6) shows the details of the strut, and the included table gives some of the important dimensions. A tapped hole on the top face allows the strut to be clamped to the inlet.

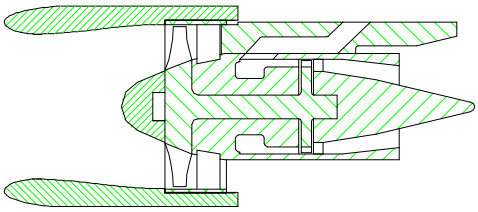

CTOL Subsonic Inlet

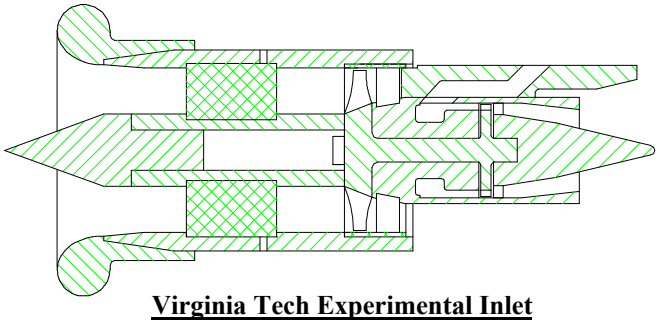

Virginia Tech Experimental Inlet

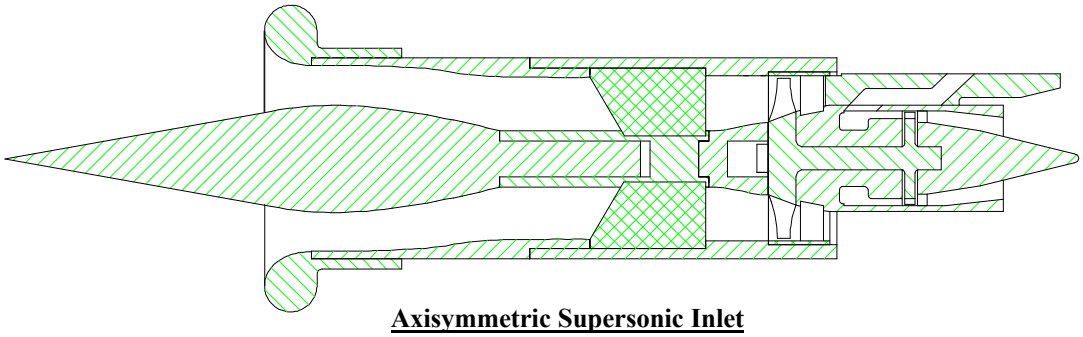

Axisymmetric Supersonic Inlet

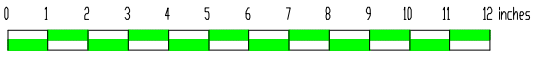

Figure 3.5. Comparison of The Experimental Inlet

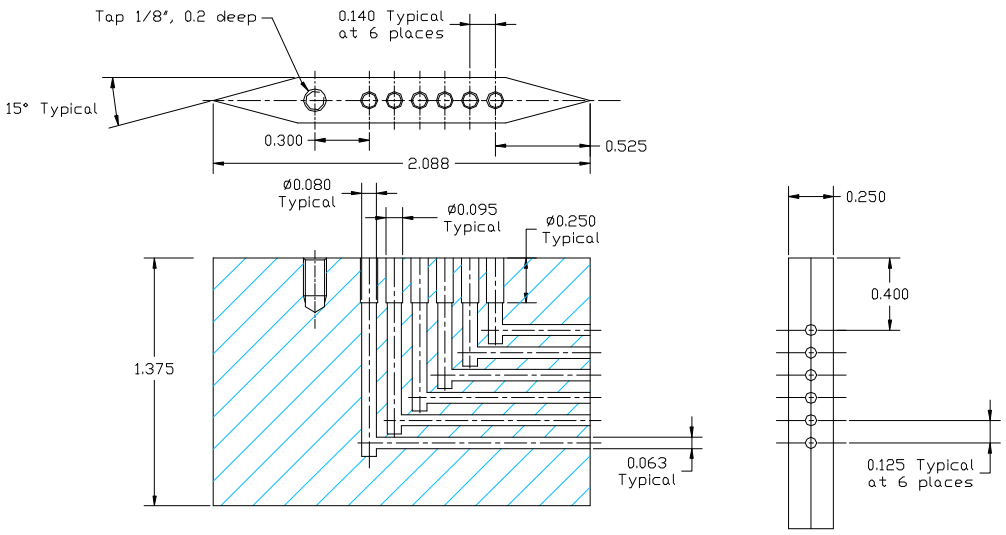

Chord Length (inches)	2.088
Thickness (inches)	0.25
Height (inches)	1.375
Number of Blowing Holes	6

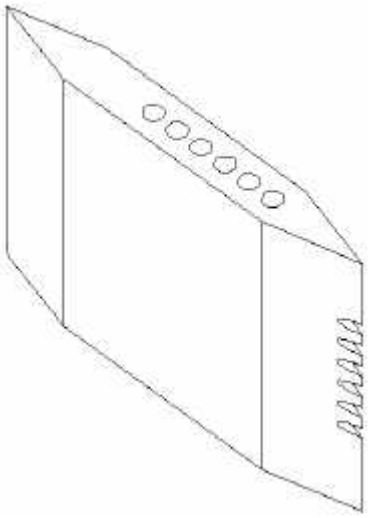

Figure 3.6. Strut Geometry & Dimensions

The geometry of these struts is very similar to those used by Leitch (1997), except for the trailing edge geometry. The trailing edge is sharp having the effect of reducing the far-field sound levels for the baseline case with no trailing edge blowing. The trailing edge is provided with six blowing holes. Because of the sharp trailing edge, the blowing holes create a crenellation as they open out on the trailing edge. This is expected to aid in mixing of the discrete jets and the wake. Leitch (1997) points out that reduction in tone was obtained inspite of lack of adequate wake filling at the hub. Hence the blowing holes are moved up so that in the bottom 25% of strut height the wake is not completely re-energized. Also to obtain better filling the hole centers are spaced two hole diameters apart. The blowing holes are 1/16" in diameter. Each hole is 'L' shaped and opens out at the top of the strut in a 1/8" diameter hole. This forms a lip, which allows support for the air supply tubing.

The struts are placed 1 strut chord length upstream of the plane of rotation. Spacing is governed by two observations. Literature suggests separation of at least 0.5 strut chord lengths to allow potential effects due to struts to decay. Bench tests showed that for uniform pitchwise mixing in the wake at least 0.5 strut chord lengths are required. This means that the error sensor has to be placed 0.5 strut chord lengths downstream of the strut trailing edge to ensure that the sensor would measure the mixed out wake and not the jet issuing out of the blowing hole. Placing the probe closer would result in the rotor seeing a split wake behind every strut, which will increase the unsteady loading and hence the far-field sound levels.

3.1.4 Flow Sensors

The flow sensors used are simple Pitot – static probes. The probe head diameter is 1/16" with a sensing hole of diameter 1/32" and length of 0.5". These probes are insensitive to incidence angle variations of 5^{o}. A single reference probe measures the free stream total pressure, and an error probe monitors the wake behind each strut. The inlet flow field is found to be radially uniform, and hence the use of a single error sensor for each wake is adequate. This also avoids the problem of having too many flow disturbance generators. The probes are connected to silicon micromachined pressure transducers (Lucas Nova Sensor). A differential output corresponding to the gage pressure is obtained from the transducers. The signal is converted to a single ended ground referenced signal. This is necessary, since controller elements like the Digital Signal Processing (DSP) board and the filters are ground referenced.

3.1.5 MEMS Based Microvalve

Individual control of the blowing rate of each hole is obtained by the use of MEMS based microvalves. The microvalves used for this research are NO-3000 Fluistor^{TM}, supplied by Redwood Microsystems. The microvalves are Normally Open (NO), i.e. if no signal voltage is applied the microvalves are fully open and operate at maximum flow rate as governed by the source pressure. The design specifications are given in Table (3.1) below. Figure (3.7) shows two views of the microvalve and the external dimensions and pin connections. Included in this figure is the principle of operation of the microvalves. The microvalve operates on the thermo-pneumatic principle. The actuator is a sealed cavity, which holds the control liquid inside it. One wall of the cavity is a diaphragm,

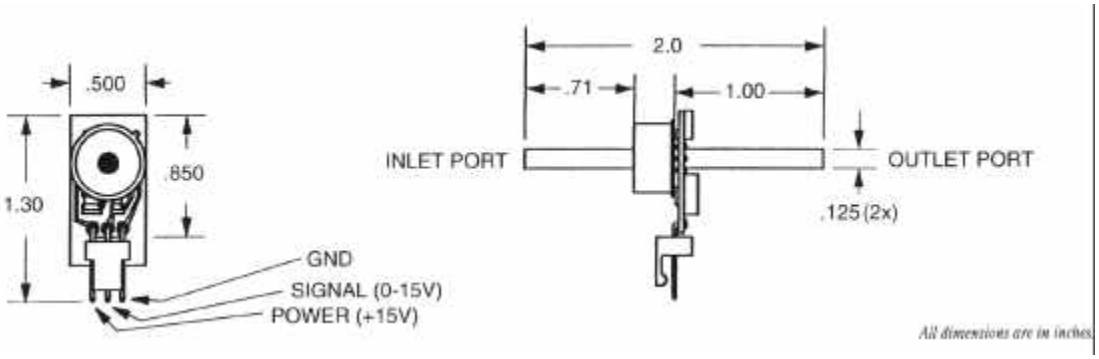

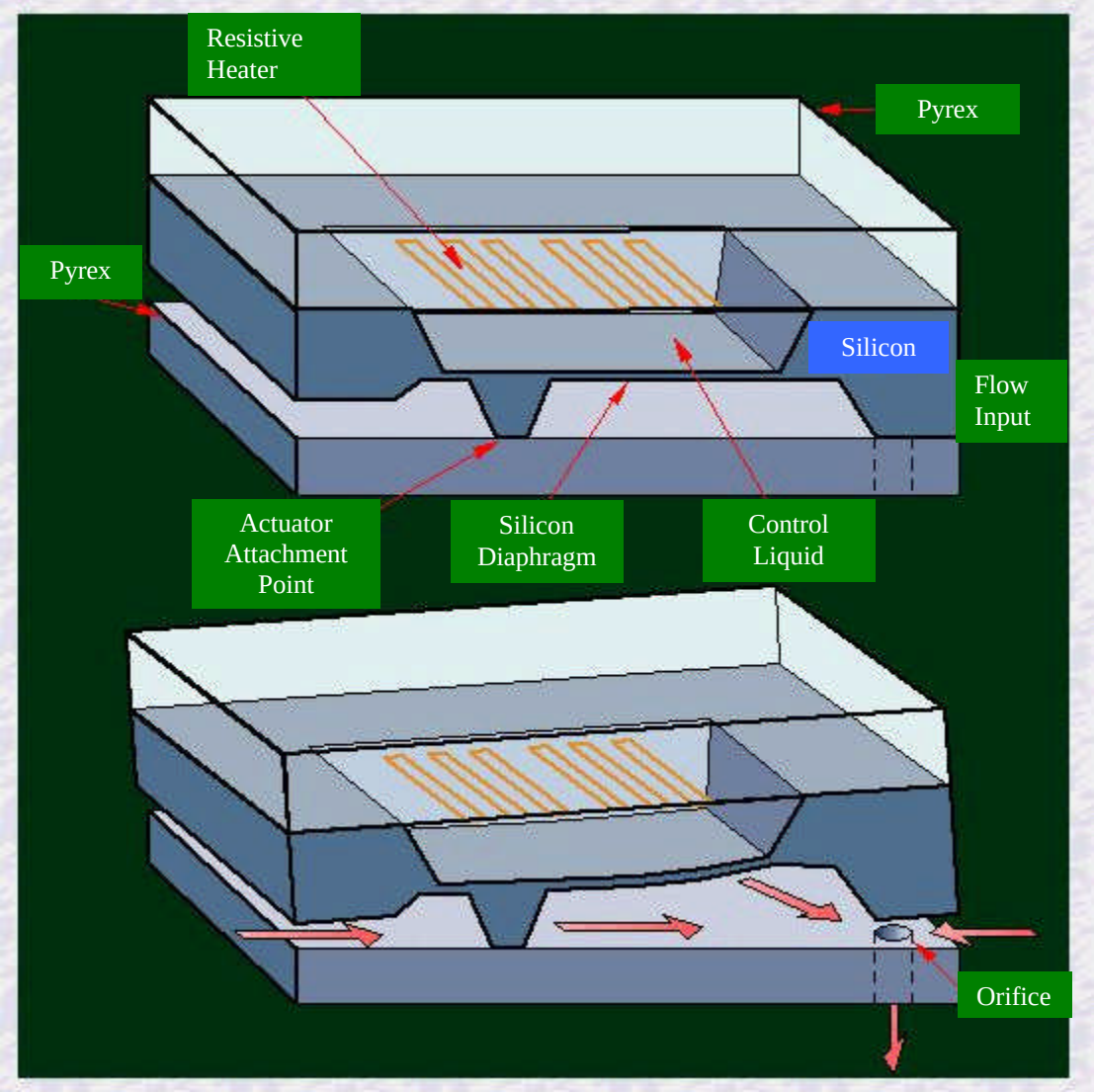

Figure 3.7. Microvalve. Dimensions & Operation (Ref: Redwood Microsystems)

which flexes when the cavity pressure increases due to evaporation of the liquid. A thin – film resistor provides the heat required for vaporization. The flexing of the diaphragm wall is translated into valve movement. Thus flow rate is governed by varying the signal voltage, for a Normally Open valve, from 0 – 15 volts.

Table 3.1. Microvalve Specifications

Fluid Media	Non – corrosive gases
Outlet Pressure Range	0 – 100 psig
Maximum Supply Pressure	100 psig
Proof / Burst Pressure	150 / 250 psig
Flow Rate Range. (Based on Nitrogen @ 25 psid and 25^{o} C)	0.2 sccm to 3000 sccm
Response Time (0-100% Full scale rise time)	500 ms typical
Average Power Consumption (at 50% flow capability)	700 mW
Operating Temperature Range	0 – 40 C
Signal Voltage	0 – 15 Volts
Power supply	15 Volts (0.250A peak, 0.100A continuous)

3.1.6 Active Controller

The controller used in this research was developed by Feng (1998) as part of his doctoral research. A brief explanation of the controller follows. The controller is a Proportional Integral Differential (PID) feedback controller. It has Multiple Input Multiple Output (MIMO) capabilities. In the experiments, the controller accepts four error signals as

input, and outputs four control signals to the microvalves. The flow sensors, described previously, generate the error signals. The controller operates to minimize the error signal by opening or closing the microvalves. A single control signal is generated for each strut, which is applied to all six microvalves. The controller employs the Least Mean Square (LMS) technique.

3.2 Research Facility

This section describes the facility and instrumentation used for the acoustic testing. Figure (3.8) shows a schematic of the entire facility for testing and Figure (3.9) is a photograph of the actual setup, taken prior to testing.

3.2.1 Anechoic Chamber

The Virginia Tech Anechoic Chamber is a facility maintained by the Vibrations and Acoustics Laboratory. An anechoic chamber simulates free-field environment. To achieve this acoustic waves radiated from a source placed in the chamber must be absorbed, rather than reflected. This objective is met by constructing the walls, ceiling, and floor of the chamber with wedges of sound absorbing material. A false floor made with metal grating provides for a steady, weight bearing work surface. The anechoic chamber measures $13.1 \times 8.9 \times 6.6$ ft ($4.0 \times 2.7 \times 2.0$ m), and is constructed with Owens Corning Type 705 industrial fiberglass wedges. Each of these wedges is 3.0 ft (0.91 m) thick. The Virginia Tech facility is considered anechoic above 200 Hz, with an ambient

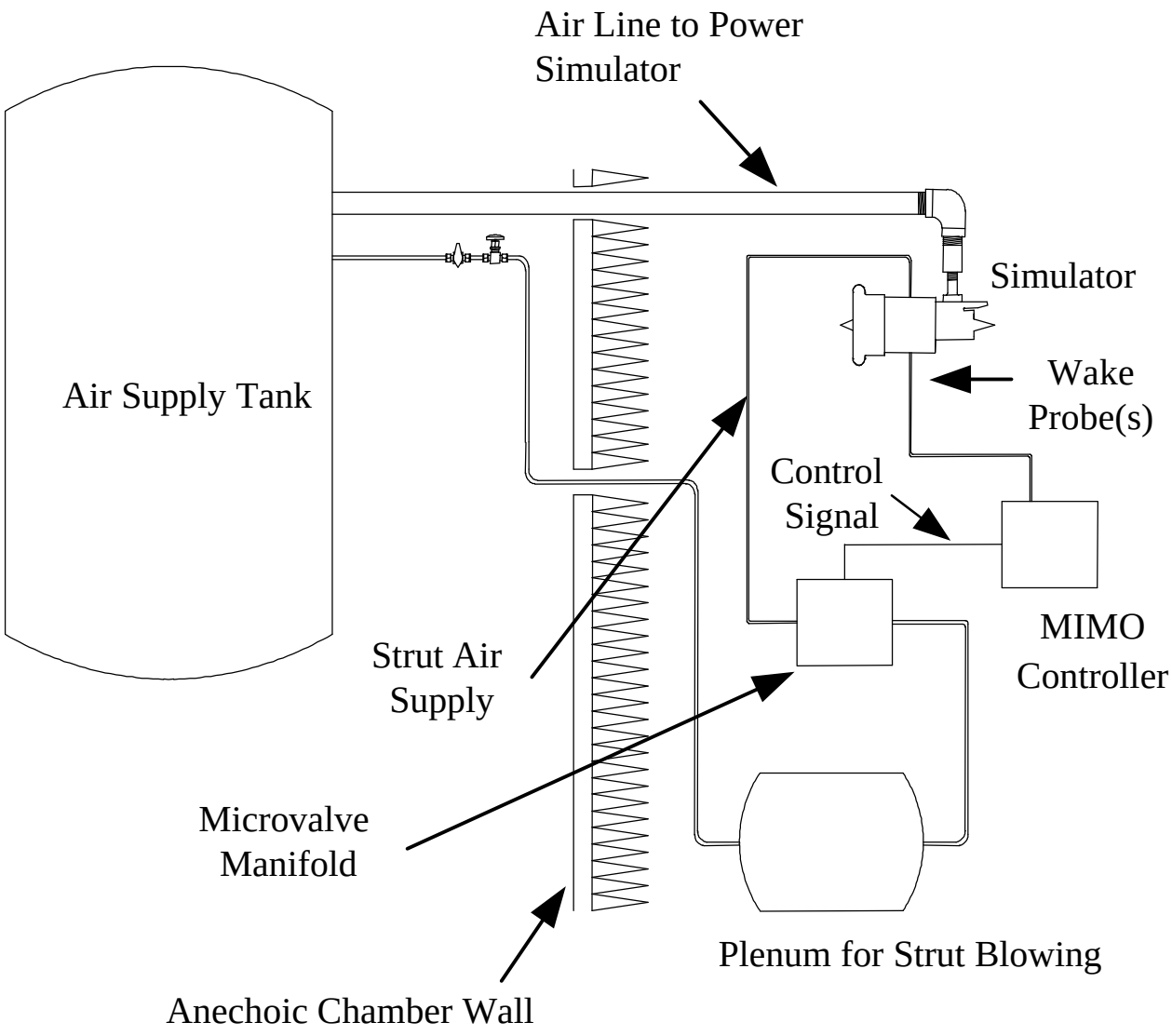

Figure 3.8. Schematic of Test Facility

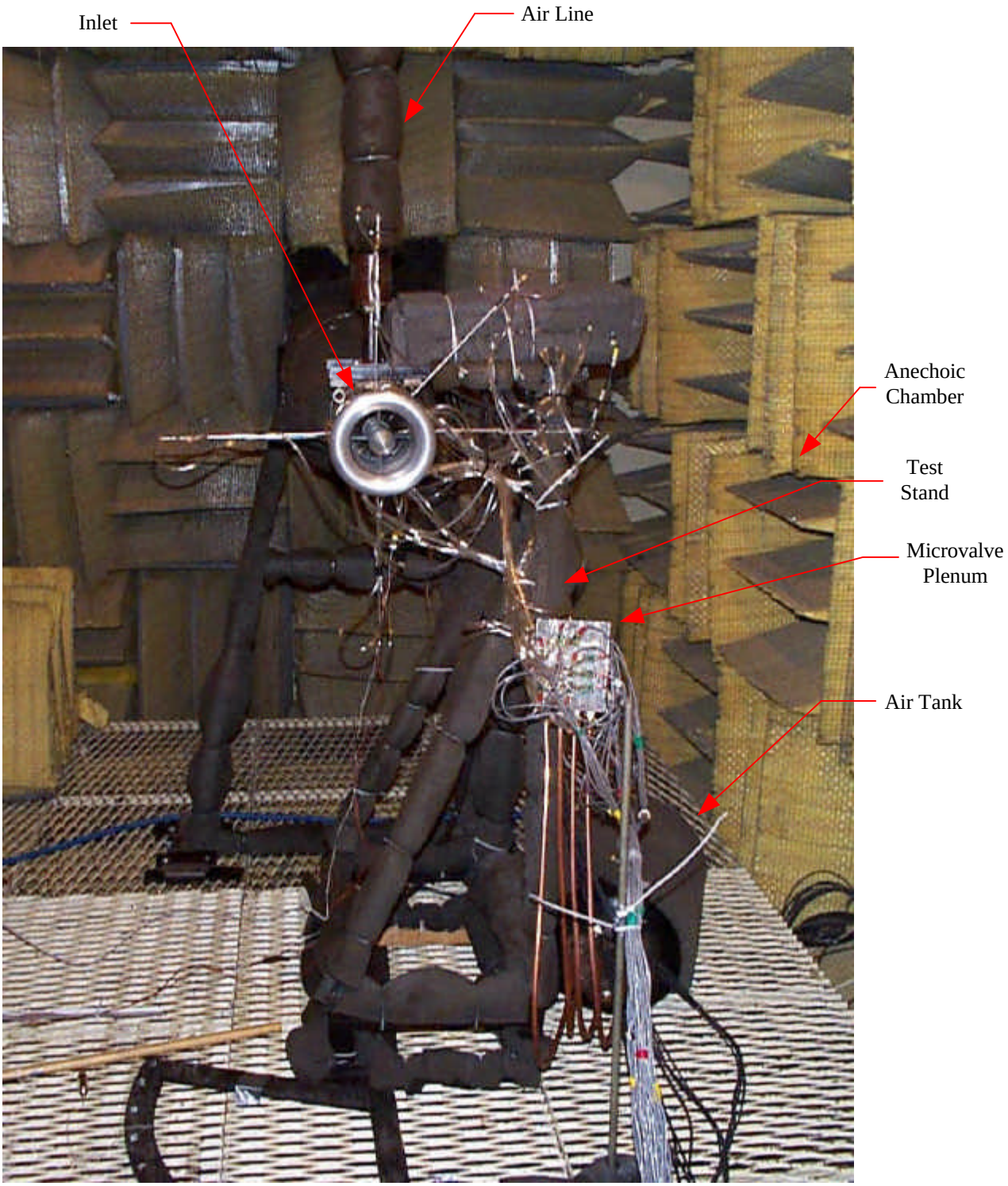

Figure 3.9. Research Facility

noise level of approximately 30 dB. This ambient noise level does not affect the measured noise levels during testing, since minimum in-test noise levels are above 70 dB. An acoustically treated door normally closes the chamber. However for the purpose of this research, it was necessary to modify the door with a 1.5 ft (0.45 m) diameter circular opening to provide the fan with a continuous air supply. All objects inside the chamber were covered with 1" thick acoustic foam to maintain the anechoic quality of the chamber.

3.2.2 Test Stand

The tests carried out in the anechoic chamber are static tests i.e., the forward flight of the engine is not simulated. For this purpose, a test stand made from angle irons, with a top plate for mounting the simulator is used. The simulator is mounted onto the test stand with two ¼" bolts. The stand is placed at the center of the chamber, with the axis of the simulator 48 in (1.2 m) above the elevated floor. This is done to avoid ingestion of ground vortices, which would add to inlet distortions. A 2" diameter air line is flange mounted to the top plate, and sealed with a cork gasket. This air line provides the high pressure air to power the simulator. The inlet slides onto the simulator fan shroud and is held in place by a cowl. The cowl runs the length of the simulator and forms an exhaust duct for the turbofan discharge. An orifice plate is placed inside the cowl and located using set screws. Loading of the turbofan is controlled by the area of the annulus formed by the orifice plate with the turbine exhaust duct. The turbine exhaust is ducted separately from the fan exhaust so as not to affect the fan loading. Well downstream of the simulator exit, the exhausts from the turbine and fan are mixed in the exhaust pipe. The exhaust

pipe is 12” in diameter, made from sheet metal, and exhausts turbine and fan air into the atmosphere.

3.2.3 Compressed Air Supply

Compressed air is required not only to power the simulator but also to supply blowing air. The compressed air is carried by a main line that is 2” in diameter. It is fitted with a solenoid valve that serves as an emergency shut-off. Two ball valves, one of them a full ported valve, are used in tandem for simulator speed control. During the testing speed control was achieved to within 50 rpm on either side of the desired speed. Pressure gages on the main line help in monitoring the line pressure and the turbine inlet pressure. A 1” line from the main supply line taps off air required for blowing. The air is routed to a supply plenum placed in the chamber. An air regulator mounted on the feed line maintains plenum pressure. Four pipes connect the supply plenum to a manifold. The manifold is a block of aluminum with four ¼” holes drilled into it. Each hole has six tapped holes. Microvalves were mounted in these holes using Swagelok fittings. Each microvalve is connected to a single blowing hole on a strut through Tygon tubing. Care is taken to ensure that each joint is leak proof.

An Ingersoll-Rand four-stage reciprocating compressor meets the compressed air requirements. The compressed air facility is equipped with an activated-alumina drying unit and a heat exchanger. This ensures that the compressed air that drives the turbine is free of water vapor and also at room temperature.

3.2.4 Instrumentation & Data Acquisition

The instrumentation for aerodynamic error sensing has been described in Section (3.1). This section will briefly explain the acoustic sensors used and the data acquisition system. A ¼" Bruel and Kjaer condenser microphone, Model 4136, is used to record the acoustic field of the turbofan. The microphones have a linear response up to 30 KHz. The microphone is mounted on a Bruel and Kjaer preamplifier. A battery powered Bruel and Kjaer power supply is used to power the microphone and amplify the acoustic signal. A HP 35665A dual channel signal analyzer processes the acoustic data. A Bruel and Kjaer pistonphone is used to calibrate all microphones used. The pistonphone generates a 94 dB SPL at 1 KHz. The pistonphone is mounted on the microphones using an adaptor for sealing, and the microphone signal is recorded in the analyzer. This sets the level of the microphone signal to 94 dB. The spectrum is also saved for later use in obtaining the frequency data for purpose of graphing. Acoustic measures are inherently unsteady, since the microphone measures the time history of the acoustic pressure at its face. Hence the acoustic data recorded is an average of 15 spectra. Furthermore seven readings are recorded at each position, and five closely grouped readings are averaged. It is this average that is reported in the directivity plots. The overall sound pressure level is also recorded. The time histories of the error signals, and the control signals are recorded using a National Instruments data acquisition board (AT-MIO-64E). The data acquisition is controlled by a program written in LabVIEW.

3.3 Test Procedure

This section describes the test procedure followed for the acoustic testing. The procedure for aerodynamic bench tests is included in Appendix (A). The primary testing involved measuring the far-field directivity at the two test speeds of 29,500 rpm, and 40,000 rpm, with and without trailing edge blowing. Figure (3.10) shows the map of measured locations. In total, twelve positions are measured in the horizontal plane, from 0^{o} - 110^{o}, with consecutive positions being 10^{o} apart. Since the inlet used is symmetric, the measured directivity holds for corresponding positions in the vertical plane, and also in the mirrored horizontal plane. The 0^{o} position lines up with the axis of the simulator. However, before these tests could be conducted it was important to fix the speeds at which simulator is to be run. Starting at 25,000 rpm acoustic data is recorded and analyzed every 1,500 rpm. To be able to measure the success of trailing edge blowing it is necessary to have the BPT peak considerably above the broadband noise. It is also important to be able to control the simulator speed during testing. From these two considerations the lower speed of 29,500 rpm is fixed. The higher test speed is fixed by the limiting flow capacity of the microvalves. During the speed check, time history of the control and error signals is acquired and analyzed to see the speed at which the control signal saturates at 0 V, without completely minimizing the error signal. This behavior is observed at a speed slightly in excess of 40,000 rpm, and hence the higher speed is set at 40,000 rpm.

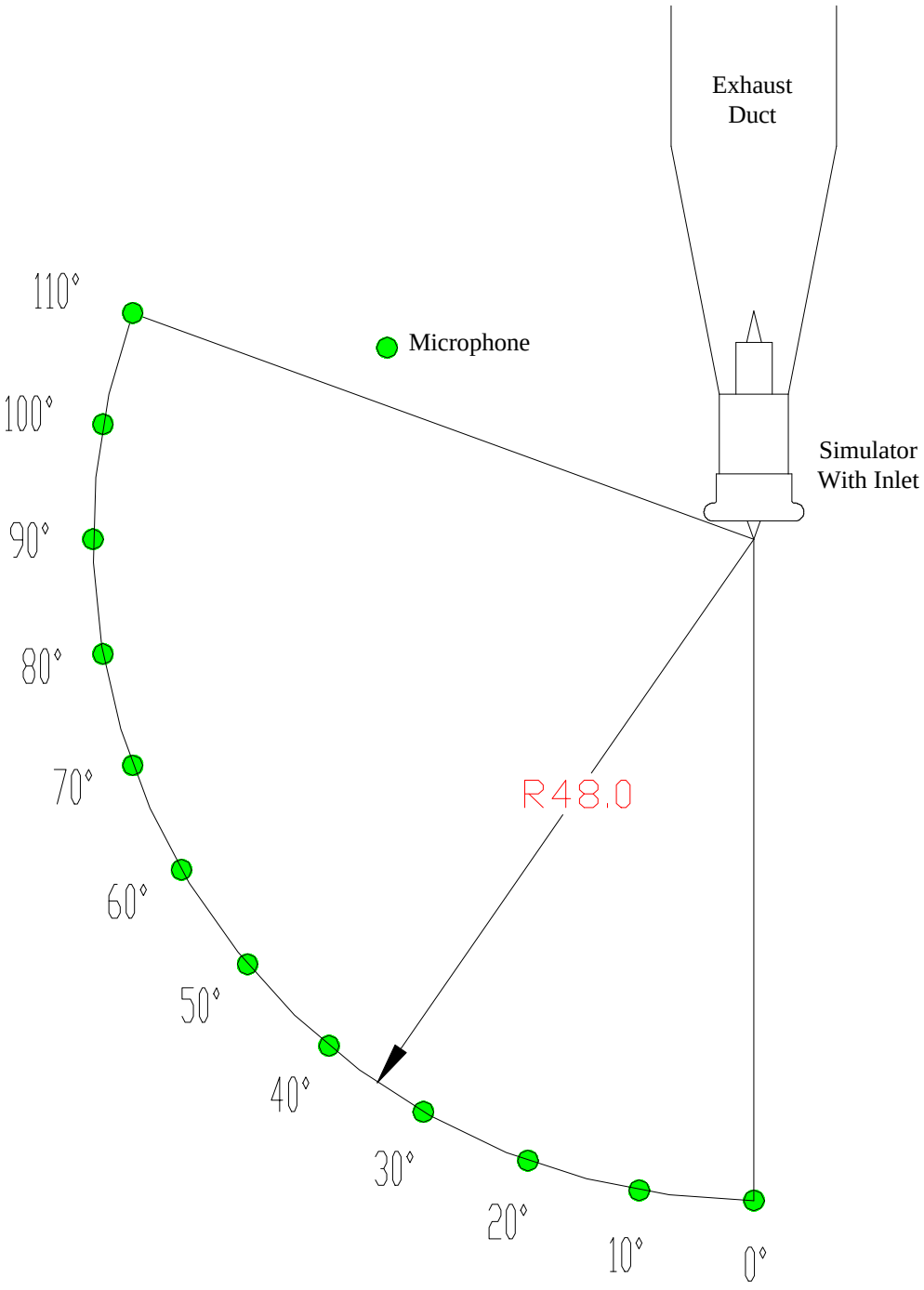

Figure 3.10. Far-Field Directivity Map

Chapter 4

Results and Discussion

This chapter presents and discusses the results obtained from the aerodynamic and acoustic testing. The chapter is divided into four sections. Section 1 discusses the aerodynamic results obtained from the blower bench tests. Results from bench tests involving a demonstration of active control form Section 2. Section 3 discusses the acoustic results. Section 4 consists of a modal analysis, and calculation of sound power. Modal analysis of the transmitted field is used to interpret some of the important features of the radiation directivity. Sound power levels are evaluated from the obtained data to better understand the effect of wake management.

4.1. Aerodynamic Results

This section presents the aerodynamic results obtained from the bench tests performed on the strut, described in Section (3.1.3). The aerodynamic results are presented in the form of 2-D contour plots, in Figure (4.1). The X-axis is the pitchwise direction, nondimensionalized by the strut thickness. The Y-axis is the spanwise direction, nondimensionalized by the strut height. The contours display the ratio of the axial velocity to the maximum free stream velocity. The choice of maximum free stream velocity is made to assign a common base for all ratios, and also to bring out the variations that exist in the flow field. Also seen in these plots are two vertical lines at

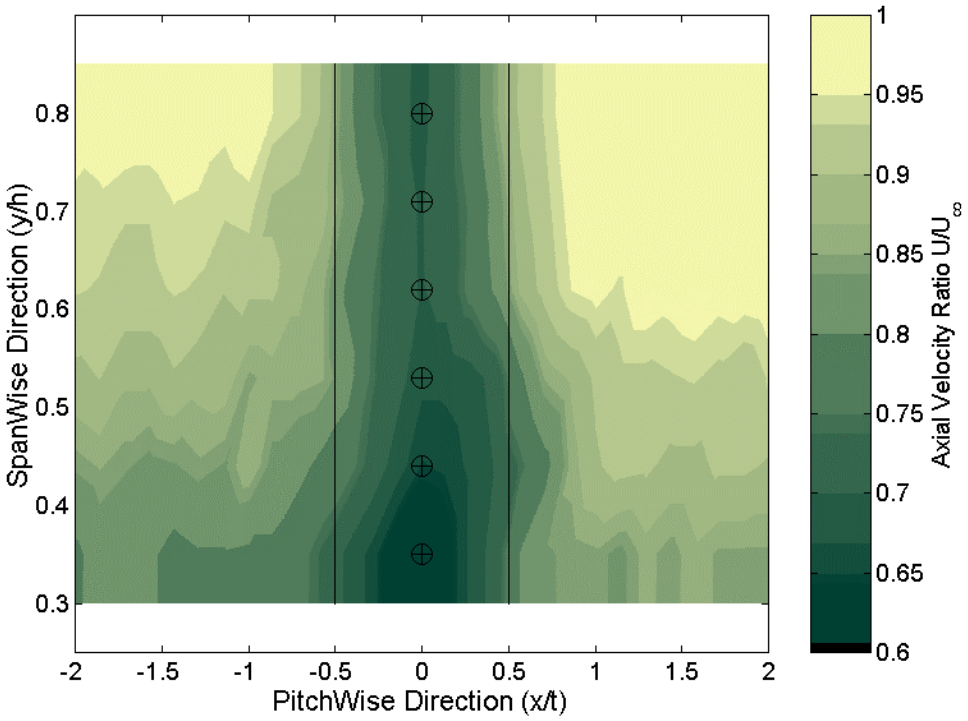

Figure (4.1a). Without TEB

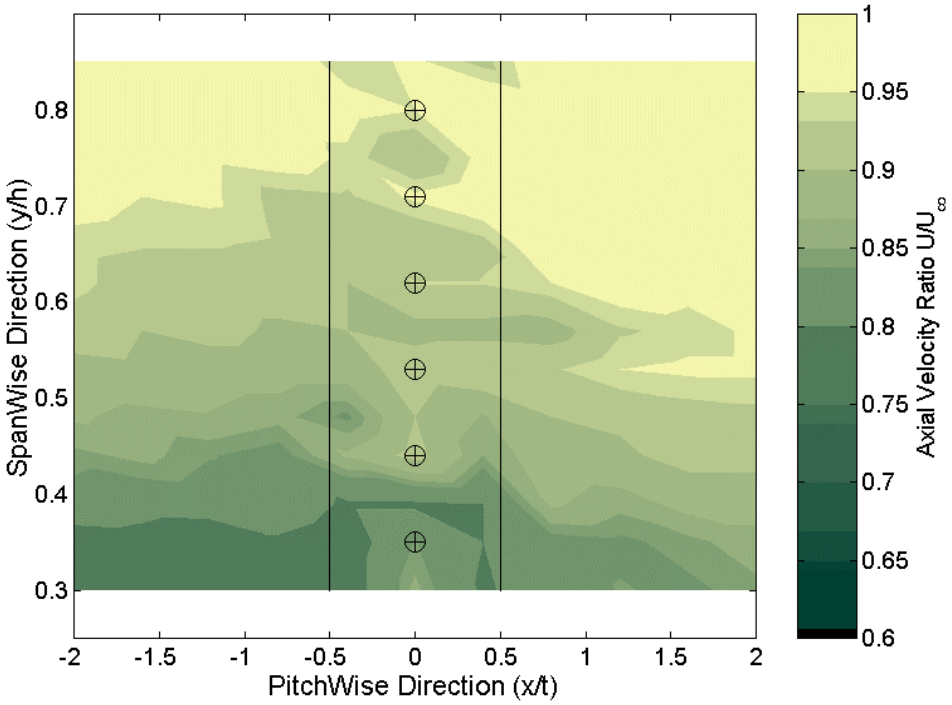

Figure (4.1b). With TEB

Figure (4.1). Axial Velocity Ratio Distribution at 0.5Cs

± 0.5, representing the maximum thickness of the strut. The circles with crosshairs represent the location of the trailing edge blowing holes.

The aerodynamic results presented are obtained using the bench setup as described in Appendix (A). The flow field is measured using Pitot-static probes. The traversed area is 1" x 1.2", with no measurements made close to the endwalls. The trailing edge of the strut lies at the center of the traversed width. On the contour plots the X-axis origin locates the trailing edge. Also the span of the traverse is restricted to the region bounding the blowing holes. Data is acquired 0.5 strut chord lengths downstream of the strut, with and without blowing.

Figure (4.1 a) is a velocity contour plot of the baseline case, i.e. without trailing edge blowing. The wake is centered about the trailing edge of the strut, as seen by the maximum velocity defect occurring at the X-axis origin. The free stream axial velocity is not uniform in the spanwise direction, being slower closer to the hub. This produces a wider wake, with a greater velocity defect, closer to the hub. As discussed in Section (2.1.2), if the rotor inflow contains circumferential variations, acoustic energy is radiated due to increased fluctuation of the lift force at the blade surface. Furthermore, the circumferential velocity defect is not uniform in the spanwise direction. This leads to increased source strength and hence greater far-field sound levels at the blade passing frequency and its harmonics.

Figure (4.1 b) shows the velocity ratio contours with the application of trailing edge blowing. The data is acquired after the blowing rate of each blowing hole is optimized. The blowing rate is optimized when the total pressure in the wake equals the free stream total pressure. Two Pitot-static probes are used to optimize the blowing rate. Both probes

are located at the same axial distance downstream of the strut, with the probe axes in the horizontal plane formed by the axis of the blowing hole, the blowing rate of which is being optimized. One of the probes measures the free stream total pressure, which is the reference signal. The other probe is located behind the trailing edge of the strut, and measures the maximum velocity defect generated by the strut. The plenum pressure is maintained constant, at 85 psig, and the microvalve signal voltage is adjusted, by potentiometers, until both the probes read the same total pressure. This procedure is repeated at all six blowing hole locations, so that at every spanwise location the total pressure behind the strut trailing edge equals the free stream total pressure at the same spanwise location. The procedure followed above emphasizes the advantage of individual control in the presence of spanwise variations in free stream axial velocity. By optimizing the wake filling at discrete spanwise locations the potential of overfilling, which is as undesirable as the wake, is avoided. Furthermore, the close spacing of the holes ensures adequate spanwise mixing as observed by the wake filling obtained between the blowing holes. At most spanwise locations the wake velocity is equal to or varies in small amount with the axial velocity in the free stream at the same span. In addition, the spanwise variation of axial velocity in the wake is very similar to that in the free stream. If the rotor inflow is circumferentially smooth, as described by this contour plot, then the magnitude of the fluctuations of the lift force at the blade surface decrease, reducing the far-field sound levels. Theoretically, the absence of circumferential velocity variations implies that the rotor noise is only due to steady loading.

4.2. Demonstration of Active Control

In this section results from preliminary experiments with active control are shown. The results shown were obtained during studies conducted to set control parameters. They serve to highlight the advantages of the current configuration due to the flexibility of adapting to global changes.

Figure (4.2) presents the time histories of free stream total pressure, free stream static pressure, wake total pressure, and control signal. This experiment involved placing the fully assembled inlet, as shown in Figure (3.1), over the intake of a centrifugal blower. Flow information is obtained from the Pitot-static probes. The data acquisition begins at time t = 0. The blower is started after 10 seconds, as observed from the trace of the free stream static pressure, which begins to drop. The error signal can also be seen, as the total pressure in the wake falls below the free stream total pressure. For the sake of clarity only one error signal and the corresponding control signal are shown on this graph. The controller is activated 10 seconds after the blower is started. It should be noted that initially the signal is set to 12 V to ensure that the normally open microvalves are fully closed. The control signal drops instantaneously, causing the microvalves to open. The error signal approaches the reference, as the axial velocity in the wake increases. The controller converges after about 15 seconds. At time t = 60 seconds, a step change in the inlet flow field is effected, by changing the discharge conditions of the blower, causing an increase in mass flow. The free stream static pressure drops suddenly, accompanied by a corresponding change in the error signal, as the total head loss increases. The controller responds, causing the microvalve to open, and converges after about 8 seconds.

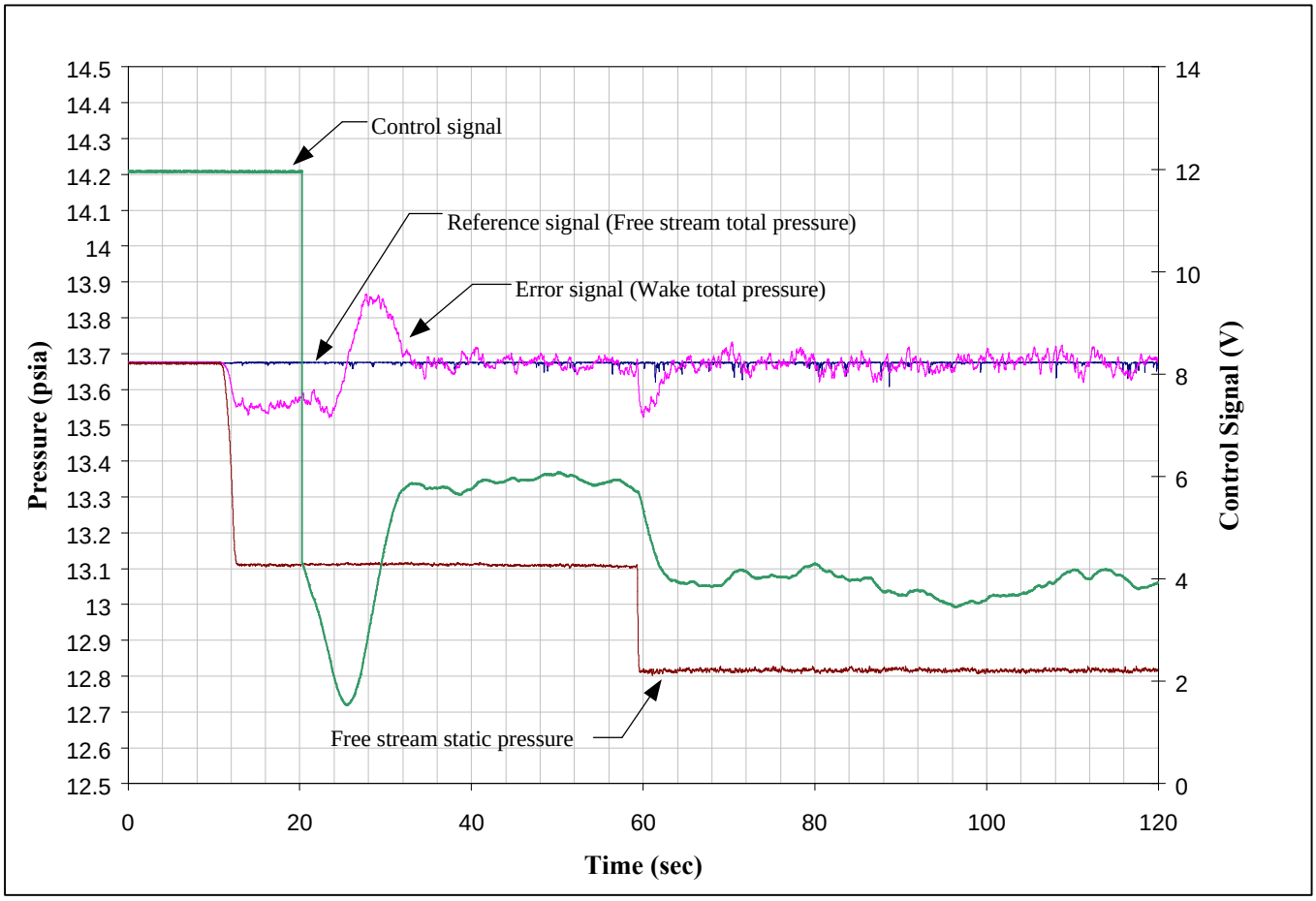

Figure 4.2. Time Histories of Pressure & Control signal

4.3. Acoustic Results

The acoustic data acquired, as described in Section (3.3), are presented in this section. Both tabulated data, as well as directivity plots are shown. The results are presented for the two tested speeds, 29,500 rpm and 40,000 rpm. The data presented consists of the recorded sound pressure levels at the blade passing frequency and the first harmonic, and the overall sound pressure level. While the directivity plots show the radiation patterns with and without trailing edge blowing, the tabulated form shows also the reduction. Figure (4.3) shows sample far-field acoustic spectra acquired at the 20^{o} microphone location at a simulator speed of 29,500 rpm. These spectra were recorded with the signal analyzer frequency range set to 51.2 kHz to observe the effect on the higher order harmonics. The spectra shown represent the sound radiation with and without blowing. Reductions at all harmonics of the BPF can be seen. As expected the sound pressure level is the greatest at the blade passing frequency. The stator-rotor spacing ensures that only the first few harmonics contribute significantly to the far-field sound, and hence the reduction in the levels of subsequent harmonics of the baseline spectrum. The spectrum with trailing edge blowing shows that inspite of the reduction, the first harmonic peaks above the broadband noise. It is possible that the rotor interaction with the **E**xit **G**uide **V**anes (EGV's) contributes significantly to the far-field noise at the first harmonic. The broadband noise levels do not change appreciably, as expected.

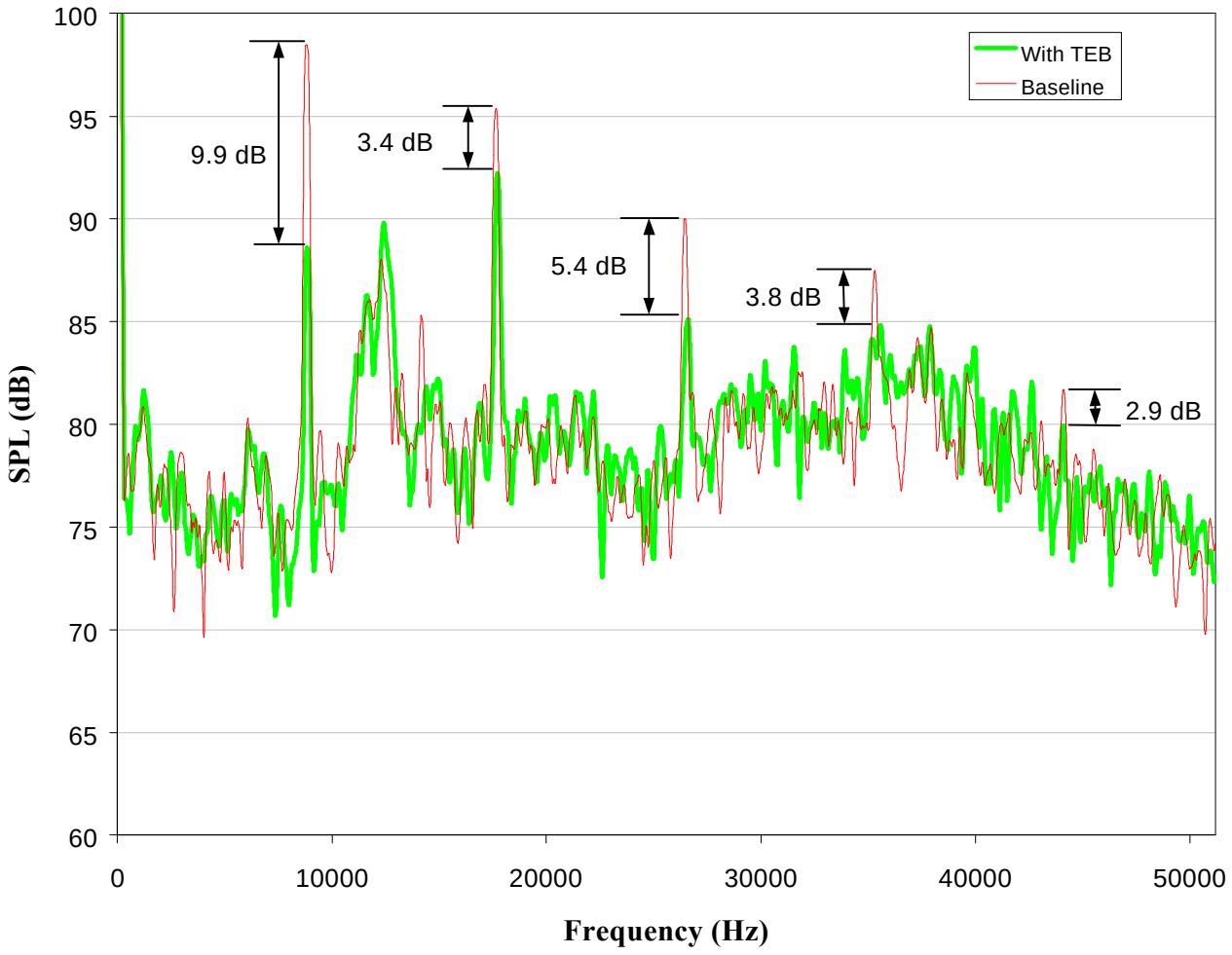

Figure 4.3 Far - Field Acoustic Spectra @ 20^{o} and 29,500 rpm

4.4.1 Speed 29,500 rpm

Figure (4.4) and Table (4.1) present the acoustic data recorded at a simulator speed of 29,500 rpm. Figure (4.4 a) shows the directivity pattern of the blade passing tone. As observed, the blade passing tone shows reduction at all recorded positions, except at 0^{o}, which lines up with the axis of the simulator. The plane wave mode is the only mode that has a maximum along the axis of the simulator, and can exist for interaction of the rotor with the struts, as well as the downstream EGV's. The average reduction recorded in the BPT is 5.5 dB, with a maximum reduction of 8.2 dB at the 20^{o} position. Significant reductions, greater than 3 dB, are obtained at most positions.

Figure (4.4 b) shows the radiation directivity of sound pressure level at the first harmonic. In this case the reductions are confined to the sector $20^{o} – 50^{o}$, inclusive. The average reduction in this sector is 3.7 dB, with the maximum reduction of 6.1 dB at the 20^{o} position. The increase observed outside of this sector could possibly be due to unmasking of other modes. The far-field directivity depends on the combined radiation of all generated modes, including interference effects. Trailing edge blowing reduces the amplitude of modes propagating due to stator-rotor interaction. The destructive interference of these modes with modes generated by other mechanisms is affected by this amplitude reduction. This would cause the sound pressure level to increase along certain directions.

The overall sound pressure level (OASPL) does not exhibit any significant change over most of the measured positions, as shown by Figure (4.4 c). This is expected since trailing edge blowing is beneficial only in reducing the tones, which contribute in small

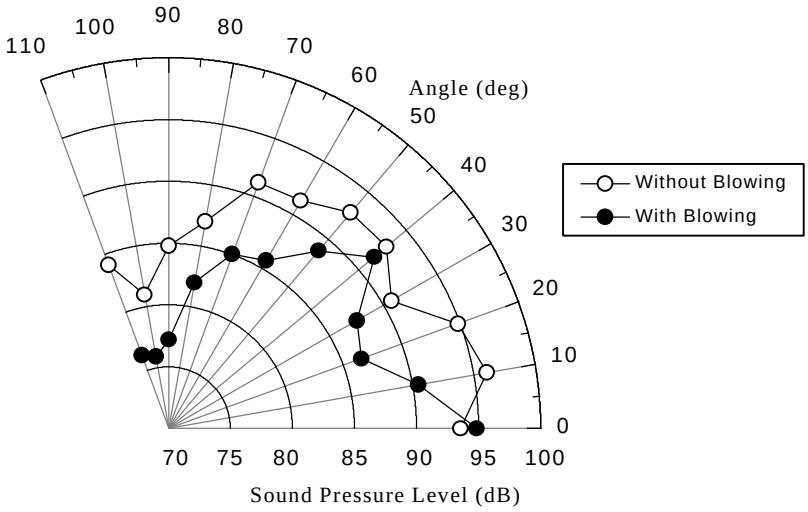

a. Blade Passing Tone

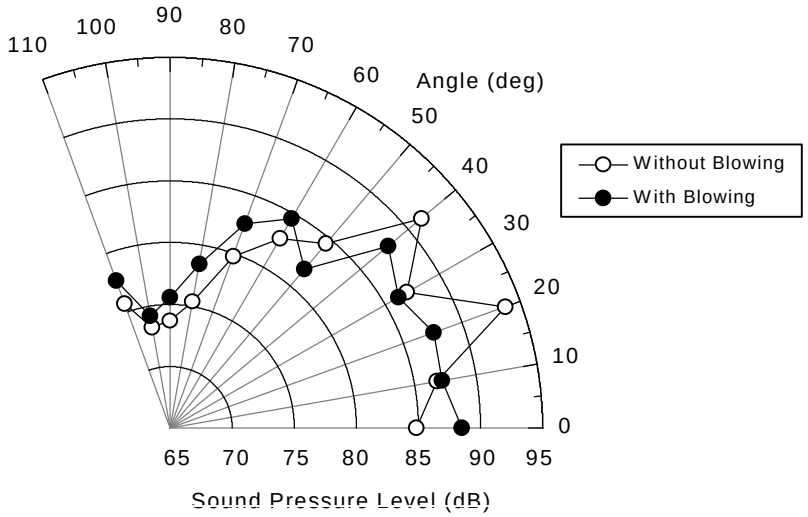

b. First Harmonic Tone

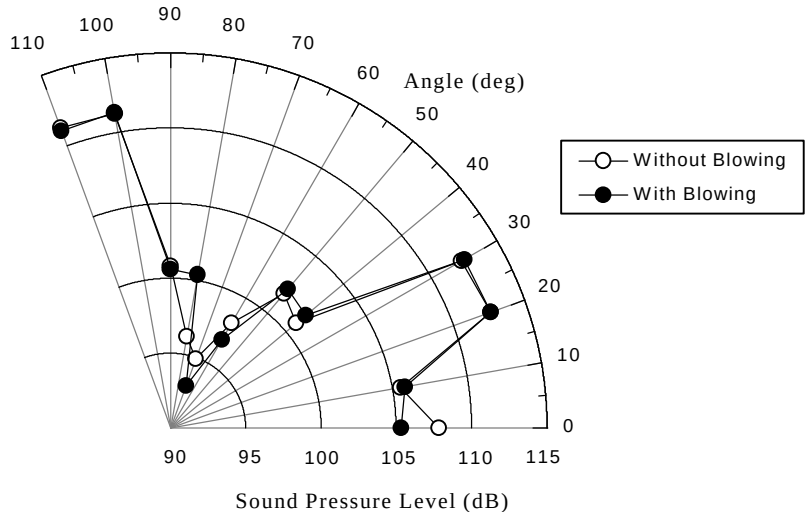

c. OverAll Sound Pressure Level

Figure 4.4 Far - Field Directivity Plots for 29,500 rpm

Table 4.1. Acoustic Results at 29,500 rpm

Sound Pressure Level at the Blade Passing Frequency			
29,500 rpm			
Angle	Without Blowing	With Blowing	Reduction
0	93.5	94.8	-1.4
10	96.0	90.4	5.6
20	94.8	86.5	8.2
30	90.7	87.5	3.2
40	92.9	91.6	1.2
50	92.8	88.8	4.0
60	91.3	85.7	5.7
70	91.2	85.0	6.2
80	87.0	82.0	5.0
90	84.8	77.2	7.6
100	81.0	75.9	5.1
110	84.1	76.3	7.8
Average	91.77	88.42	5.54

Sound Pressure Level at the First Harmonic			
29,500 rpm			
Angle	Without Blowing	With Blowing	Reduction
0	84.8	88.5	-3.8
10	86.8	87.2	-0.4
20	93.7	87.6	6.1
30	87.0	86.2	0.8
40	91.4	87.9	3.5
50	84.5	81.8	2.7
60	82.7	84.6	-1.8
70	79.8	82.6	-2.8
80	75.4	78.5	-3.1
90	73.7	75.6	-1.9
100	73.3	74.2	-0.9
110	75.7	77.7	-2.0
Average	86.74	84.84	0.80

Overall Sound Pressure Level			
29,500 rpm			
Angle	Without Blowing	With Blowing	Reduction
0	107.8	105.3	2.5
10	105.5	105.8	-0.3
20	112.6	112.6	0.0
30	112.3	112.5	-0.2
40	100.9	101.7	-0.8
50	101.7	102.1	-0.5
60	98.1	96.8	1.3
70	94.9	93.0	1.8
80	96.2	100.4	-4.2
90	100.8	100.6	0.2
100	111.3	111.4	-0.1
110	111.3	111.1	0.2
Average	108.08	108.02	0.25

part to the energy content of the spectrum. However it must be reiterated that the objectionable noise is from the tones and the tonal reductions are perceived.

4.4.2 Speed 40,000 rpm

Figure (4.5) and Table (4.2) present the acoustic data recorded at a simulator speed of 40,000 rpm. As shown in Figure (4.5a), the blade passing tone shows reduction in the sector 0^{o} to 40^{o}. The average reduction over all measured positions is 2.7 dB, with a maximum of 7.3 dB at 20^{o}. In the sector 60^{o} to 110^{o} it can be observed that the sound pressure level remains the same, with and without trailing edge blowing. Figure (2.2) shows the trend of far-field directivity as the frequency changes. As seen, with increase in the frequency the number of lobes in the far-field increase and the principal lobe shifts towards the axis. In addition, the sideline radiation exhibits a broad pattern, which is typically generated by higher order modes. Thus, from Figure (4.5 a), it can be inferred that for the setup used, the lower order loading harmonics contribute more to sound radiation at the blade passing frequency. In support of this is the rapid decrease in the sideline sound levels, and the disparity with the levels recorded in the forward arc.

The first harmonic levels exhibit reductions at most positions, as shown in Figure (4.5b). The sound pressure level at 20^{o} increases by 3.2 dB after trailing edge blowing. This could be due to unmasking of modes due to other interaction mechanisms. The peak reduction is 3.1 dB at 30^{o}. The far-field directivity is a result of interaction of modes due to two interaction mechanisms, stator-rotor and rotor-egv interactions. Also, with the increase in frequency more modes are cut-on. This complex interaction is reflected by the fact that the reductions at the first harmonic are not as significant as the BPT reductions.

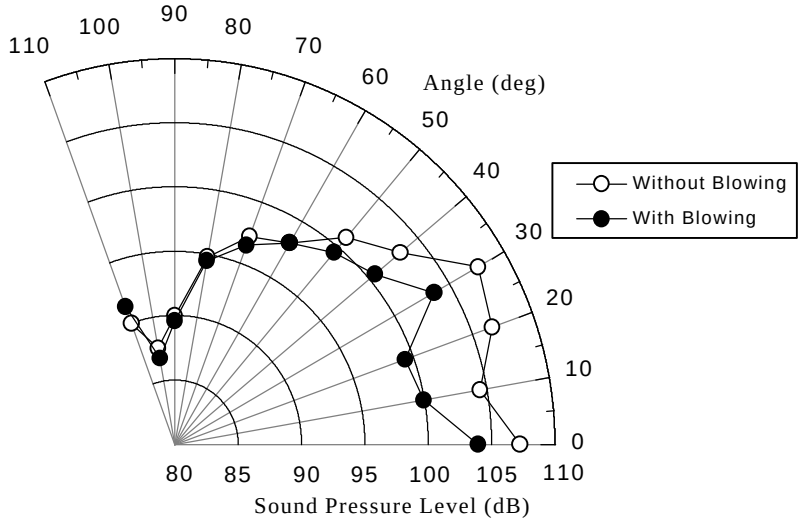

a. Blade Passing Tone

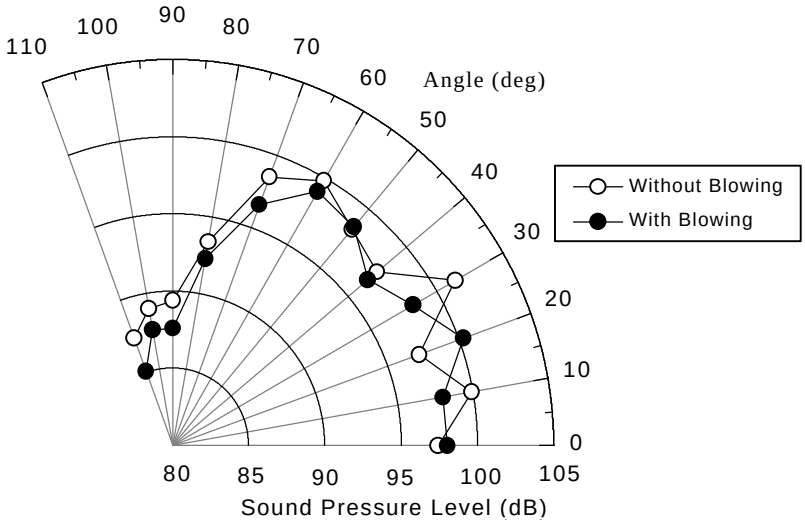

b. First Harmonic Tone

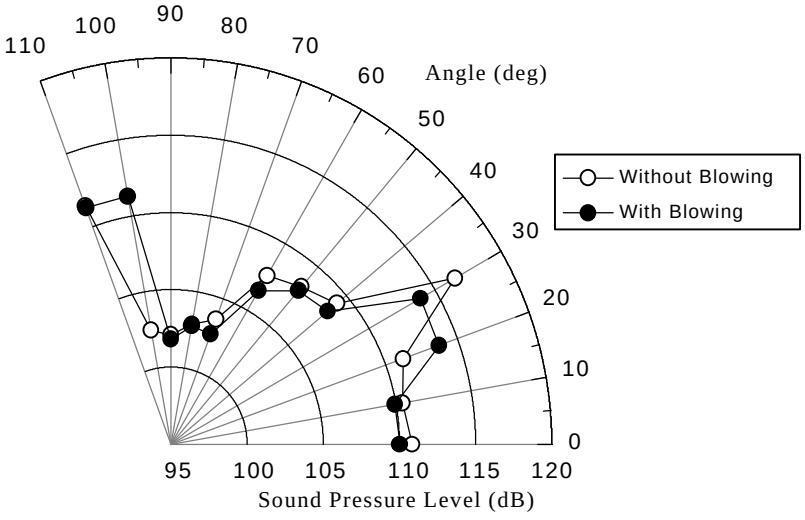

c. OverAll Sound Pressure Level

Figure 4.5. Far - Field Directivity Plots for 40,000 rpm

Table 4.2. Acoustic Results at 40,000 rpm

Sound Pressure Level at the Blade Passing Frequency			
40,000 rpm			
Angle	Without Blowing	With Blowing	Reduction
0	107.2	103.9	3.3
10	104.4	99.9	4.6
20	106.6	99.3	7.3
30	107.6	103.6	4.0
40	103.2	100.6	2.5
50	101.0	99.5	1.4
60	98.1	98.1	0.1
70	97.2	96.5	0.6
80	94.8	94.5	0.4
90	90.0	89.6	0.3
100	87.6	86.8	0.8
110	90.0	91.4	-1.3
Average	102.90	99.33	2.69

Sound Pressure Level at the First Harmonic			
40,000 rpm			
Angle	Without Blowing	With Blowing	Reduction
0	97.4	98.0	-0.6
10	99.9	98.0	1.9
20	97.2	100.3	-3.1
30	101.4	98.2	3.1
40	97.5	96.7	0.7
50	98.3	98.5	-0.2
60	99.8	99.0	0.8
70	98.5	96.6	2.0
80	93.4	92.3	1.1
90	89.4	87.6	1.8
100	89.0	87.6	1.3
110	87.4	85.1	2.3
Average	97.52	96.80	1.19

Overall Sound Pressure Level			
40,000 rpm			
Angle	Without Blowing	With Blowing	Reduction
0	110.8	110.0	0.8
10	110.4	109.9	0.5
20	111.2	113.7	-2.5
30	116.5	113.9	2.6
40	109.2	108.4	0.7
50	108.3	108.0	0.2
60	107.6	106.5	1.1
70	103.6	102.6	1.0
80	102.9	102.8	0.1
90	102.1	101.8	0.3
100	102.5	111.3	-8.8
110	111.4	111.3	0.1
Average	110.09	109.92	0.25

The directivity plot of the OASPL is shown in Figure (4.5c). The overall sound pressure level does not change much over most of the points, except for an increase of 8.8 dB at the 100^{o} position. The reason for this increase is not known yet at this point.

4.4.3 Comparison of directivity patterns at 29,500 rpm & 40,000 rpm

Figure (4.6) compares the directivity patterns for the baseline case at the two tested speeds. As is expected, the increase in speed causes an increase in the far-field discrete frequency sound levels. This occurs due to an increase in the magnitude of the fluctuating lift force at the rotor, caused by a steeper velocity profile. The steeper velocity profile arises due to the fact that as the inlet flow Mach number increases, so does the velocity deficit caused by the strut. This can be observed in Figure (4.2), wherein the baseline wake total pressure deficit increases with Mach number. A comparison of the directivity of the blade passing tone, Figure (4.6a), shows that the speed change has significant effect in the forward arc of 0^{o} to 50^{o}. The minimum increase in the blade passing tone levels is 8 dB. The average increase in this sector is 11.8 dB, while the average increase over the entire map is 11.8 dB.

Figure (4.6b) compares the directivity of the first harmonic level at the two speeds. The minimum increase in the first harmonic tone is 11 dB, neglecting the 20^{o} to 40^{o} positions. As seen in the figure, the change is greater for sideline levels. In fact, while the average increase is 11.8 dB over all the measured points, in the sector 60^{o} to 110^{o} the average increase is 14.0 dB. When compared to the average increase in the blade passing tone, it can be inferred that as the speed increases, the amount of energy radiated at the first

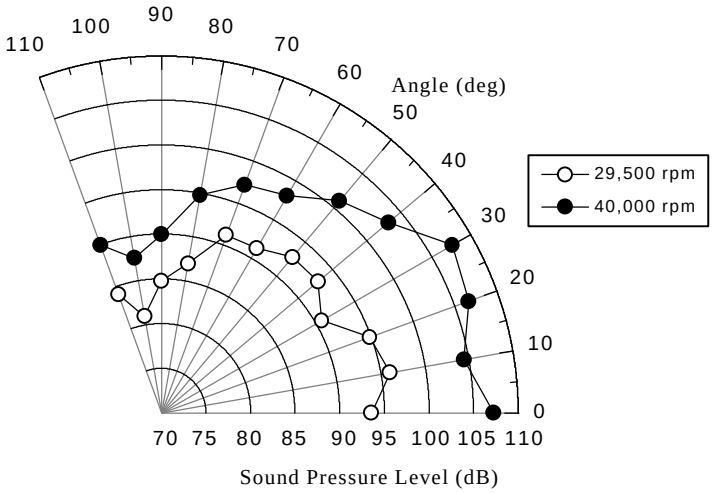

(a). Blade Passing Tone

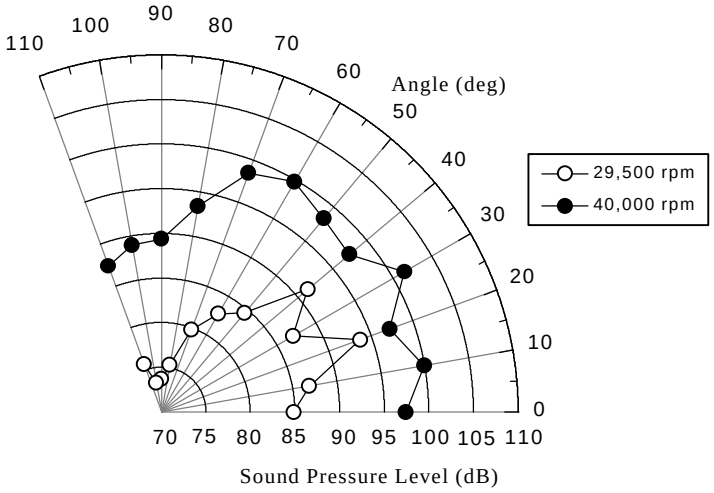

(b). First Harmonic Tone

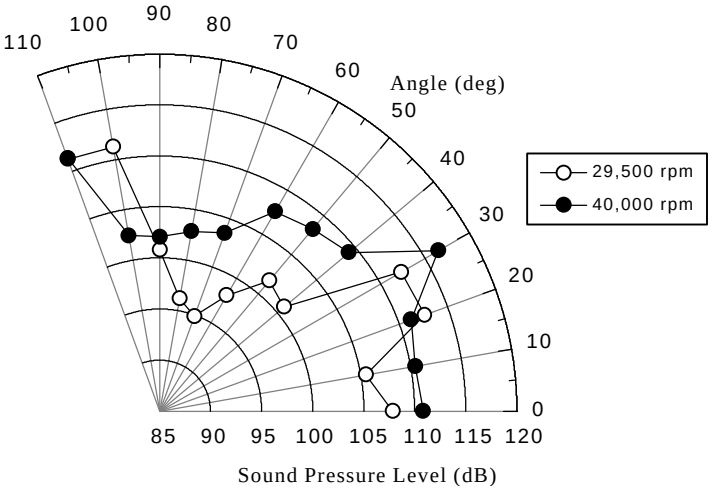

(c). Overall Sound Pressure Level

Figure 4.6. Comparison of Baseline Far-Field Directivity

harmonic increases significantly. This is because at a higher speed the circumferential variations provide a greater number of loading harmonics, while the increase in frequency causes more modes to cut-on. The comparison of the overall sound pressure level is shown in Figure (4.6 c). The change in the levels is not as dramatic as that seen for the blade passing tone, or the first harmonic. The average increase is only 2.0 dB. This suggests that the sources causing broadband noise did not change significantly with speed. Appendix (D) contains all the recorded spectra, at both speeds and with and without blowing.

4.4. Analysis

The analyses presented in this section consist of the modal analysis and a calculation of the sound power from the obtained directivity. The interpretation of the results of these analyses allow better understanding of the effect of trailing edge blowing, and sheds some light on the obtained results.

4.4.1 Modal Analysis

In this section the results of a modal analysis are presented and discussed. Sample calculations are shown in Appendix (B). A summary of the modal structure due to the various interactions is shown in Table (4.3). Implicit in carrying out this analysis is the assumption of absolute symmetry in the flow field due to the obstructions present. However, since small differences will exist, the analysis serves only as a guide to

Table 4.3. Modal Analysis - Cut-on Modes and Principal Radiation angles

Frequency f, Hz	Circumferential Order, m	Radial Order, n	Principal lobe angle, ψ_P, deg
STATOR - ROTOR INTERACTION			
8850	2	0	19
		1	51
8850	6	0	61
17700	4	0	18
		1	31
17700	8	0	34
		1	54
12000	2	0	14
		1	35
	6	0	40
		1	78
24000	4	0	13
		1	22
		2	34
		3	51
	8	0	24
		1	37
		2	49
		3	66
ROTOR - EGV INTERACTION			
17700	10	0	43
		1	72
12000	8	0	56
24000	10	0	30
		1	45
		2	59
8,850	BPF at 29,500 rpm		
17,700	First harmonic at 29,500 rpm		
12,000	BPF at 40,000 rpm		
24,000	First harmonic at 40,00 rpm		

interpreting the directivity pattern obtained. The effect of the flow distortion due to the probes is neglected, since in comparison to the struts they form a very small obstruction. The probes are located behind the top two holes. This ensures that the obstruction is restricted to the stem diameter of 1/16", and hence it is assumed that the wake shed by the probe does not produce significant unsteadiness at the rotor. However, the most significant effect of the probes might be on the modal structure. The probes will not form identical wakes, and hence they might excite modes due to fundamental loading harmonics ranging from 1 per rev - 5 per rev. In the present analysis the generated modes are calculated using 4 per rev distortion pattern for the stator-rotor interaction, and the rotor-stator interaction is due to wakes from 18 rotor blades impinging on 26 exit guide vanes (egv). Another factor that allows only approximate interpretation from the analysis is the resolution used to obtain the directivity.

At 29,500 rpm, the principal radiation angles of modes cut-on at the BPF due to stator-rotor interaction are calculated to be at 19^{o}, 51^{o}, and 61^{o}. At the same frequency, the rotor-egv interaction does not have any cut-on modes. Furthermore, neither interaction mechanism excites the symmetric mode (m=0, n=0). The maximum reduction in the blade passing tone at 29,500 rpm is obtained at 20^{o}, which is close to 19^{o}, the principal lobe angle of mode (2,0). As discussed in Section (4.3.2), the lower order harmonics contribute more to the far-field levels. With the mode (2,0) being the lowest order mode cut-on, the maximum reduction due to trailing edge blowing is to be expected at the measured location of 20^{o}. The presence of significant sound pressure level at the 0^{o} position is possible only if the symmetric mode (0,0) is cut-on. Since the analysis predicts otherwise, the presence of this mode suggests asymmetry in the interaction mechanisms,

which is not accounted for by the analysis. For the stator-rotor interaction to produce this mode at the blade passing frequency, as constrained by Equation (2.2), the rotor blade number ought to be a multiple of 4. Manufacturing tolerances can produce such an effect, where the interaction of a group of blades with certain loading harmonics might vary from that of the entire stage. The same effect can be produced by the rotor-egv interaction. In fact this latter effect is more probable due to the high vane number of the egv stage. Again the reason for this is the dissimilarity that exists due to manufacturing tolerances.

The first harmonic modal structure at 29,500 rpm displays principal lobe angles at 18^{o}, 31^{o}, and 34^{o} due to stator-rotor interaction. Modes due to rotor-egv interaction are now cut-on, with predicted maxima at $43^{o}$and 72^{o}. Again the symmetric mode (0,0) is not produced by either interaction mechanism. The maximum reduction obtained at this frequency is at 20^{o}, which agrees with the principal lobe angle of the lowest order mode (4,0). Lesser reductions are obtained from $30^{o}$to 50^{o}, the region that contains the principal angles of the higher order modes. The increase in sound level, after trailing edge blowing, recorded at $70^{o}$and 80^{o} can be attributed to the mode (10,1) caused by rotor-egv interaction. As the Figure (2.2) shows, the sideline lobes tend to be broad, since the radiation in this zone is greatly affected by the diffraction effects at the edge of the inlet. Furthermore, the reduction in amplitudes of the modes generated by stator-rotor interaction would unmask the modes caused by other interaction mechanisms. From Figure (4.4 b) it is observed that the symmetric mode is generated and trailing edge blowing causes an increase of 3.2 dB in the sound level on the inlet axis. This strongly

suggests that the symmetric mode is generated by the rotor-egv interaction, as discussed in the previous paragraph.

The modal structure at 40,000 rpm has more modes cut-on, from both interaction mechanisms. The calculated principal lobe angles due to stator-rotor interaction are at 14^{o}, 35^{o}, 40^{o}, and 78^{o}, while the mode generated by the rotor-egv interaction has a far-field maximum at 56^{o}. The symmetric mode is not generated at this blade passing frequency. Figure (4.5 a) shows that reductions are recorded at all points in the forward sector, $0^{o} - 50^{o}$. This agrees well with the calculated principal angles, as all modes that radiate preferentially in this region are from stator-rotor interaction. From $50^{o}$to 110^{o}, there is little change in the sound pressure levels before and after blowing, and the sound levels drop appreciably. This is because the two modes that radiate principally in this sector are higher order modes, which means broad lobes and lesser energy content. The most interesting change at the higher speed is the reduction obtained on the axis of the inlet after blowing, and hence attributable to reduction of stator-rotor unsteady interaction. With the reasons for generation of the symmetric mode already established, it can be inferred that with an increase in speed the stator-rotor interaction starts dominating other interaction mechanisms.

The first harmonic at 40,000 rpm has numerous modes cut-on by both interaction mechanisms. Most of the modes radiate principally in the forward sector $0^{o} - 50^{o}$. Figure (4.5 b) shows that in this region, apart from an increase after blowing at 20^{o}, reductions are obtained at most positions. The two modes caused by rotor-egv interaction being higher order modes do not contribute significantly to far-field sound levels. The reduction

obtained on the inlet axis further supports the growing dominance of the stator-rotor interaction in the symmetric mode generation.

4.4.2 Sound Power

The results of an analysis to calculate the radiated sound power are presented. The procedure is briefly described in Appendix (C), and Equation 4.1 is used to arrive at the sound power of the source. This equation is used for calculating the sound power from the far-field acoustic pressure data, with the particle velocity being in-phase with the pressure fluctuations. Determining the sound power has the advantage that it describes the sound energy output of the source, without regard to the directivity. This provides a more direct understanding of the effect of trailing edge blowing on source strength. Again since the resolution of the recorded data is not high, this analysis can only provide an estimate and the trend of radiated power.

$$W = \frac{4\pi r^2 p_{rms}^2}{\rho c} \tag{4.1}$$

where; W is sound power in Watts

r is radius of annular ring

p_{rms} is the rms pressure in Pa

ρ is density of air in kg/m^3

c is the speed of sound in m/sec

The results are presented in Table (4.4) and show that for both tested speeds the application of trailing edge blowing is successful in reducing the sound power, at both the BPF and the first harmonic. At 29,500 rpm, the power in the blade passing tone reduces

by 64%, while the power at the first harmonic reduces by 37%. At 40,000 rpm the reduction in the blade passing tone power is 48%, while the first harmonic tone power reduces by 20%. A reduction in far-field acoustic power can be directly interpreted as a reduction of similar magnitude in the source power. As discussed in chapter 3, trailing edge blowing reduces the magnitude of the velocity defect seen by the rotor and also smoothes the velocity profile. Furthermore, this decreases the unsteady loading experienced by the blade as it passes through the wake, and hence the reduction in source strength. The BPT reduction is significant at both speeds, with the greater reduction at 29,500 rpm. At the same speed the blade passing tone power is reduced more than the first harmonic tone. This is because more energy is concentrated in the blade passing tone, and at the first harmonic the exit guide vanes do contribute in small measure to the far-field sound levels. A comparison of the blade passing tone at the two tested speeds shows lesser power reduction at the higher speed. This is because with an increase in speed the power of sources generated by the rotor-egv interaction increases.

Table 4.4. Sound Power & Power Level; Before & After Trailing Edge Blowing

	Sound Power, W	Power Level, dB
Speed - 29,500 rpm		
	Blade Passing Frequency	
Before TEB	0.01404	101.5
After TEB	0.00506	97.0
Reduction	64%	4.4
	First Harmonic	
Before TEB	0.00424	96.3
After TEB	0.00265	94.2
Reduction	37%	2.0
Speed - 40,000 rpm		
	Blade Passing Frequency	
Before TEB	0.14530	111.6
After TEB	0.07498	108.7
Reduction	48%	2.9
	First Harmonic	
Before TEB	0.06280	108.0
After TEB	0.05041	107.0
Reduction	20%	1.0

Chapter 5

Conclusions & Future Work

5.1 Conclusions

The focus of this research is to conduct an experimental study towards developing a trailing edge blowing system that can adapt to variations in flow parameters and reduce the unsteady stator-rotor interaction at all engine operating conditions. The effect of unsteady interaction measured in this research is the far-field sound pressure level. A scale model of a turbofan engine provides the acoustic source. A symmetric inlet with four support struts is mounted onto the turbofan simulator. The struts support a centerbody, and create circumferential velocity defects in the mean flow. Periodic interaction of the rotor blades with these velocity defects generates discrete frequency noise. The frequency of the generated noise depends on the number of rotor blades, and the number of wakes in the mean flow. Typically, the level of the discrete frequency tones is about 15-20 dB higher than the broadband noise generated by other fluid dynamic mechanisms. To reduce the unsteady response of the rotor blades the wakes must be re-energized, either partially or completely. Injecting mass off the trailing edge of the struts effects the re-energization. This process of wake management is called trailing edge blowing. To allow for trailing edge blowing, the trailing edge of the struts is provided with discrete holes. To enable optimum re-energizing at different mean flow

rates, the system involves active flow control. The different elements include MEMS microvalves, flow sensors and a PID feedback controller. Each blowing hole is connected to a single microvalve, and hence the microvalve sets the blowing rate of each hole. Flow sensors are used to generate error signals for the controller. The error signal is the difference between the total pressure measured in the free stream and the wake. The controller generates a signal voltage, which is supplied to the microvalves and controls the flow rate. The flow sensors enable continuous monitoring of the inlet flow conditions and the controller responds to changes, ensuring optimum wake management. The acoustic experiments are conducted in an anechoic chamber and the far-field noise levels are measured using an array of microphones.

From the results presented it can be concluded that controlling the blowing rate of each hole produces a very uniform flow field downstream of the strut. In addition to eliminating or reducing the circumferential variations, the radial gradient present in the free stream flow is maintained in the wake region after optimal filling is achieved. The ability of the system to achieve optimum wake filling when subjected to a step change in inlet flow conditions demonstrates the feasibility and advantage of active flow control. It was also demonstrated that far-field sound pressure levels at the relevant discrete frequencies are reduced by trailing edge blowing. Furthermore, the reduction in source strength caused by eliminating or decreasing the circumferential velocity defects, supports the effectiveness of trailing edge blowing in reducing unsteady stator-rotor interaction. The maximum sound level reduction is observed at the blade passing frequency of each tested speed. The maximum tone reductions obtained are 8.2 dB at 29,500 rpm and 7.3 dB at 40,000 rpm. Emitted sound power at the blade passing tone,

calculated from the measured directivity, is reduced by 64% at 29,500 rpm and 48% at 40,000 rpm.

5.2 Future Work

At various stages of this research, areas for future work were identified. These areas are mentioned along with possible research directions. The most important area of future research that will significantly affect the realization of an active flow control system is probably error sensing. The error sensors used in this research are Pitot-static probes, which themselves create a disturbance in the flow. In the present research the uniform radial distribution of axial velocity allowed the use of a single error sensor per strut to control the entire spanwise blowing rate. This also allowed minimizing the immersion depth of the probes into the flow, and hence the obstruction created. However, such probes are not a realistic instrumentation scheme for application in an actual engine. Therefore a non-intrusive error sensing capability must be developed to fully realize the potential of an active control system. The ideal error sensor would monitor the velocity defect caused by upstream obstructions, which is the cause for the unsteady interaction effects. A research effort by Feng is underway at Virginia Tech to investigate the use of casing microphones as error sensors.

A parametric study that investigates the effects of stage spacing and the response of the rotor to velocity defects at different radial locations is necessary. Stage spacing affects the degree of mixing of the blowing jet with the wake flow. Knowledge of minimum mixing length required and maximum stage spacing allowable will aid in developing configurations that achieve better mixing, possibly through the use of vortex generators.

The sensitivity of rotor unsteady response to velocity defects also changes with radius. From the acoustic viewpoint, if a rotor is subjected to a fixed velocity profile from hub to tip, the source strength at the rotor tip will be stronger. This is because the tip velocity is greater and acoustic source strength typically depends on the sixth power of a characteristic velocity. Thus it might be possible to benefit from wake management over only a portion of the blade height at the tip. This will reduce the amount of blowing air needed and the complexity of the system.

Development of MEMS technology leading to flow devices with higher flow capacity is another future work area. Probably the most needed development is the use of stators with a thicker cross section to allow for mass injection off of the trailing edge. This is undesirable from the engine weight perspective, and hence it is necessary to quantify realistically the benefits derivable. Studies that document the effect of wake management on engine performance and the use of trailing edge blowing for stall control might help in making this concept more acceptable to the gas turbine community.

References

Blake, William K., Mechanics of Flow-Induced Sound & Vibration, Academic Press Inc., 1986.

Corcoran, Timothy, "Control of the Wake from a Simulated Blade by Trailing Edge Blowing," Masters Thesis, Mechanical Engineering Department, Lehigh University, 1992.

Detwiler, K.P. "Reduced Fan Noise Radiation from a Supersonic Inlet," Masters Thesis, Mechanical Engineering Department, Virginia Polytechnic Institute and State University, Blacksburg, Virginia, April 1993.

Feng, Jinwei., Personal Communication, Virginia Polytechnic Institute and State University, Blacksburg, VA, 1998.

Goldstein, M.E., "Aeroacoustics," NASA SP-346, 1974.

Greatrex, F.B., and Bridge, R., "The Evolution of the Engine Noise Problem," Aircraft Engineering, Vol. XXXIX, pp. 6-10, February 1967

Hanuska, Carol A., "Aeroacoustic Effect of Choking at Inlet Guide Vanes in Subsoinc and Supersonic Inlets," M.S. Thesis, Virginia Polytechnic Institute and State University, Blacksburg, VA, 1998

Homicz, G. F. and Lordi, J. A., "A Note on the Radiative Directivity Patterns of Duct Acoustic Modes," Journal of Sound and Vibration, Vol. 41(3), pp. 283-290, 1975.

Kurosaka, M., "A Note on Multiple Pure Tone Noise," Journal of Sound and Vibration, Vol. 19, No. 4, pp. 453-462, December 1971.

Leitch, Thomas., "Reduction of Unsteady Stator-Rotor Interaction by Trailing Edge Blowing", M.S. Thesis, Virginia Polytechnic Institute and State University, Blacksburg, VA, 1997

Lighthill, M. J., "On Sound Generated Aerodynamically I- General Theory," Proceedings of the. Royal. Society. (London) Vol. 211A, pp. 564-587, 1952.

Model 460 Turbofan Propulsion Simulator Products Specification, Tech Development Inc., U.S. Patent 3434679.

Naumann, R. Georg, “Control of the Wake from a Simulated Blade by Trailing Edge Blowing,” Masters Thesis, Mechanical Engineering Department, Lehigh University, 1992.

Pande, A., Ng, W. F., "Effects of Struts on the Aeroacoustics of Axisymmetric Supersonic Inlets," Masters Thesis, Mechanical Engineering Department, Virginia Polytechnic Institute and State University, November 1994.

Park, W.J., and Cimbala, J.M., “The Effects of Jet Injection Geometry on Two-dimensional Momentumless Wakes,” Journal of Fluid Mechanics, Vol. 224, pp. 29-47, 1991.

Redwood Microsystems Inc., *Operating Principles- Fluistor Microvalve*, www.redwoodmicro.com/principles.html

Roger, M., “Applied Aeroacoustics,” von Karman Institute for Fluid Dynamics, Lecture Series, March 7-11, 1994.

Saunders, C.A., “Noise Reduction in an Axisymmetric Supersonic Inlet using Trailing Edge Blowing,” M.S. Thesis, Virginia Polytechnic and State University, Blacksburg, VA 1998.

Trefney, C.J., Wasserbauer, J.W. “Low-Speed Performance of an Axisymmetric, Mixed-Compression, Supersonic Inlet with Auxiliary Inlets,” NASA TP-2557, February 1986.

Tyler, J. M., and Sofrin, T.G., "Axial Compressor Noise Studies," SAE Transactions, Vol. 70, 1962.

Waitz, I.A., Brookfield, J.M., Sell, J., and Hayden, B.J., “Preliminary Assessment of Wake Management Strategies for Reduction of Turbomachinery Fan Noise,” First Joint CEAS/AIAA Aeroacoustics Conference, Munich, Germany, 1995.

Washburn, Karl B., and Lauchle Gerald C., “Inlet Flow Conditions and Tonal Sound Radiation from a Subsonic Fan,” Noise Control Engineering Journal, Vol. 31, No. 2, pp. 101-110, 1988.

Appendix A

Bench Test Setup & Operation

This appendix describes the test bench used for obtaining the aerodynamic results presented in Section (4.1). Figure (A-1) is a drawing of the bench setup. The bench consists of two parallel Plexiglas plates with the strut mounted between the plates. The assembly is completed by side supports that are fastened onto the plates by 1/8" bolts. The bench is then mounted on a wooden test stand, and this assembly is placed at the exit of a 4" x 4" nozzle that is connected to the discharge of a centrifugal blower. The bench is aligned so that the midspan of the strut lines up with the midspan of the nozzle cross section. The flow field downstream of the strut is measured using a Pitot-static probe. The probe is mounted on a traverse mechanism with three degrees of freedom. A stepper motor – leadscrew mechanism controls the pitchwise traverse. Motion in the spanwise and streamwise directions is achieved by manually rotating leadscrews. The survey of the flow field is conducted by first setting the streamwise location of the probe. Then at each spanwise position, the stepper motor is used to move the probe to discrete equispaced points in the pitchwise direction. At each point data is acquired through a National Instruments DAQ card driven by LabVIEW. This procedure is followed for both cases, with and without blowing. For the results shown in Section (4.2) the probe location was maintained constant through out the testing. The probe is located such that its center is

collinear with the center of a blowing hole. Introducing a sudden blockage at the inlet of the blower causes the step change in the free stream velocity.

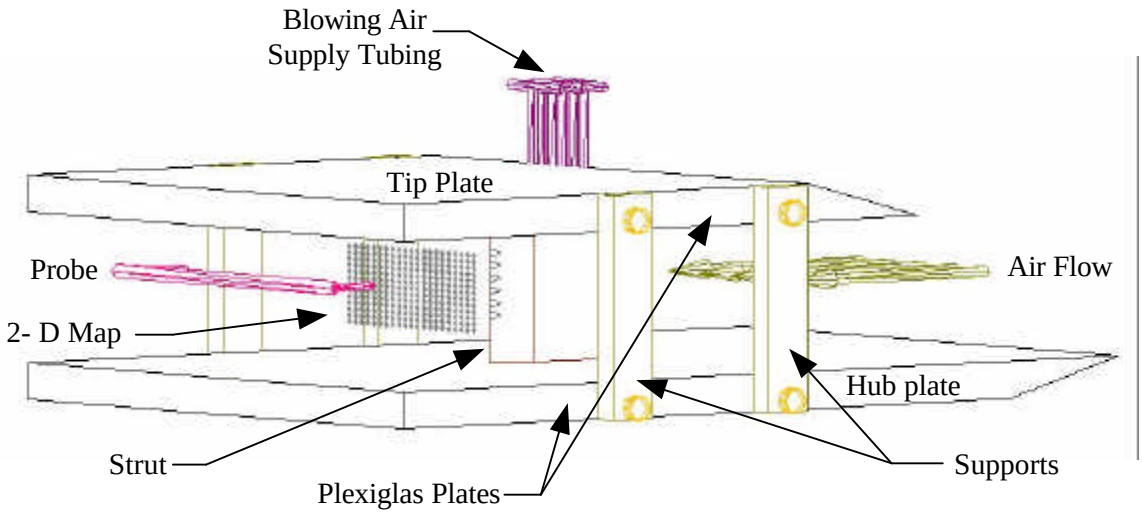

Figure A-1. Bench Test Setup

Appendix B

Modal Analysis: Sample Calculation

In this appendix a sample calculation for evaluating the circumferential modes generated by the stator - rotor interaction and the cut-off frequency of the generated modes is presented. Equation (2.2) is used to determine the generated modes and Equation (2.4) is used to decide if the mode is cut-on.

Rotor Blade Number, B = 18

Stator Vane Number, V = 4

Rotor Speed, N rpm = 29,500

Sound Speed, a in/sec = 13385.82

Tip radius, r_T in = 2.05

Hub - Tip ratio, $\sigma = 0.439$

Blade Tip Mach number, $M_T = 0.473$

Axial Mach Number, M = 0.150

Normalizing factor, $\beta = 0.989$

To obtain a circumferential mode at the BPF

Harmonic of BPF, n = 1

Loading Harmonic, k = 4

Then by Equation 2.2

Circumferential Mode Number, m = 2

For Radial Mode Number, $\mu = 0$

E-function = 2.7794 (for $\sigma = 0.439$)

Mach Number of Spinning Mode, $M_m = 4.2579$

Critical Mach Number for Spinning Mode (m, μ) $M_{mCritical} = 1.3897$

Cut - off Ratio $\varepsilon = 3.0638$

Since, $\varepsilon > 1$, this mode will propagate along the inlet and radiate into free space.

Equations used: The following equations are used, along with those already mentioned above.

$M_m = \frac{2 \pi f r_T}{a m}$, where f is the Blade Passing Frequency in Hz.

$M_{mCritical} = \frac{f_{(m,\mu)}}{m}$, where $f_{(m,\mu)}$ is the E-function

$\varepsilon = \frac{M_m}{M_{mCritical}}$

Appendix C

Sound Power: Sample Calculation

In this appendix a sample calculation for evaluating the sound power and power level from the far-field directivity is presented. The tabulated data in Section (4.3) gives the sound pressure level (SPL) at each measurement point in the far-field. From the SPL at a particular location, the P_{rms} can be calculated using Equation (C.1).

$$P_{rms} = P_{ref}\sqrt{10^{(L_P/10)}} \qquad \text{(C.1)}$$

Where; P_{rms} is the root mean square pressure in Pa

P_{ref} is the reference pressure $2x10^{-6}$ in Pa

L_p is the measured sound pressure level in dB

Since the measurements are made in the far-field, the particle velocity is assumed to be in phase with the pressure disturbance. This allows the calculation of the sound intensity at the measured location using Equation (C.2).

$$I = \frac{P_{rms}^2}{\rho c} \qquad \text{(C.2)}$$

Where; P_{rms} is the root mean square pressure in Pa

I is the sound intensity in W/m^2

ρ is the air density in kg/m^3

c is the speed of sound in air in m/sec

Sound power for a simple monopole source is obtained by integrating the sound intensity over the surface area of a sphere with the source at the center of the sphere. This is possible since the far-field sound pressure of the simple source is the same in all directions. However, the mouth of the inlet cannot be considered as a simple source, and hence the intensity at each discrete point is integrated over the surface area of a ring, as shown in Figure (C-1). The radius of the ring is distance of the microphone from the inlet mouth. The width of the ring subtends an angle of 10^{o} at the center of the ring. This assumes that the SPL measured at a particular angle is uniform over the width of the ring, and hence the calculated sound power is only approximate in quantity. Equation (C.3) is used to calculate the sound power. Summing the sound power at each ring gives the total sound power and Equation (C.4) is used to calculate the sound power level from the total sound power.

$$W = I(4\pi r^2) \qquad \text{(C.3)}$$

Where; W is sound power in Watts

r is the far-field radius at which the directivity is measured in m

$$L_W = 10\,\mathrm{Log}_{10}\left(\frac{W_T}{W_{ref}}\right) \qquad \text{(C.4)}$$

Where; L_W is the sound power level in dB

W_{ref} is the reference power 10^{-12} in Watts

W_T is the total sound power in Watts

The calculated values at 30^{o} for the no blowing case are given below;

P_{rms} = 0.68396 Pa

I = 11.695×10^{-4} W/m^{2}

W = 9.52×10^{-4} W

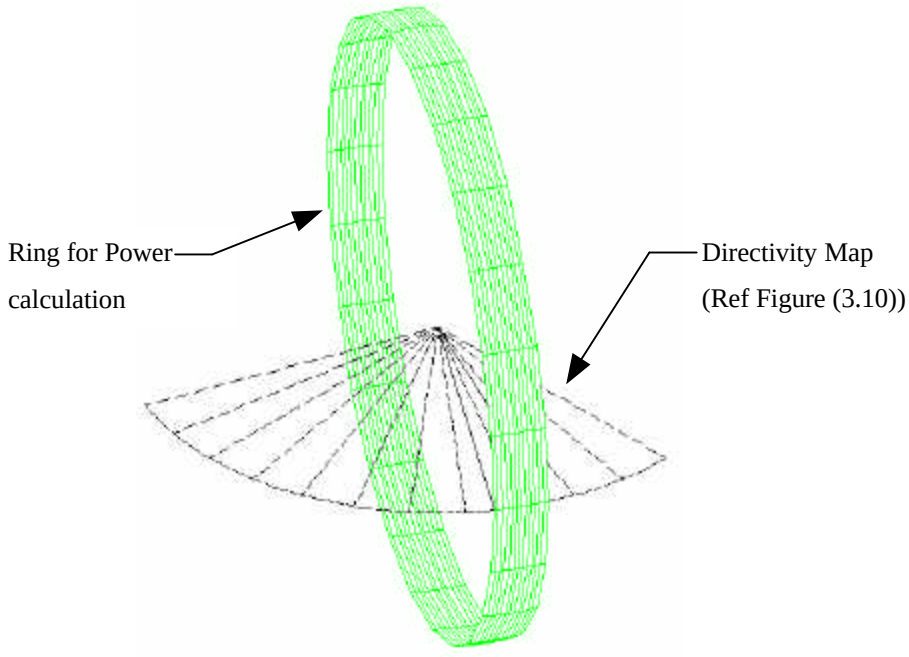

Figure C-1. Surface Area for Sound Power

Appendix D

Acoustic Spectra

This appendix contains the spectra obtained during the acoustic testing. The data are presented in two sets. The first set is acoustic spectra at 29,500 rpm, with and without blowing, and at all directivity points as described in (3.3). The second set contains the same data measured at 40,000 rpm. The spectrum for "No Blowing @ 29,500 rpm & 0^{o}" is not shown as the data file was corrupted during conversion.

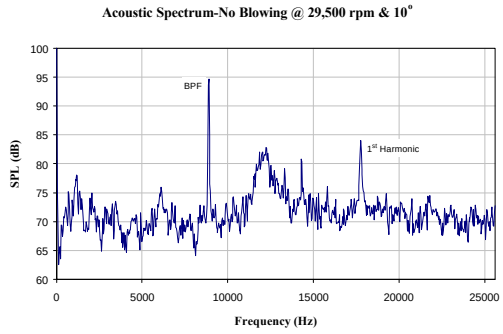

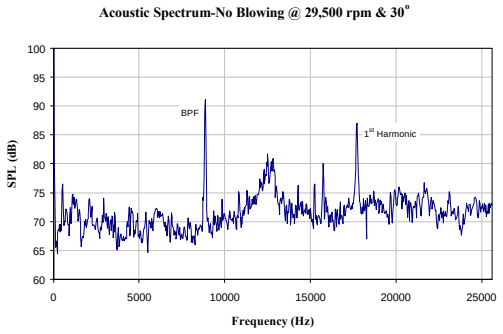

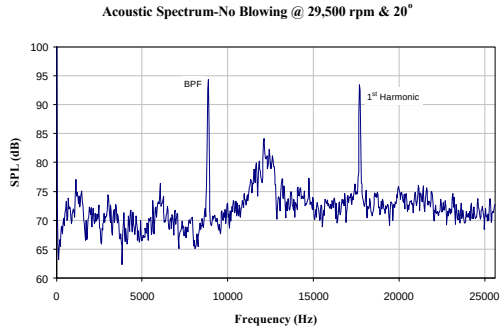

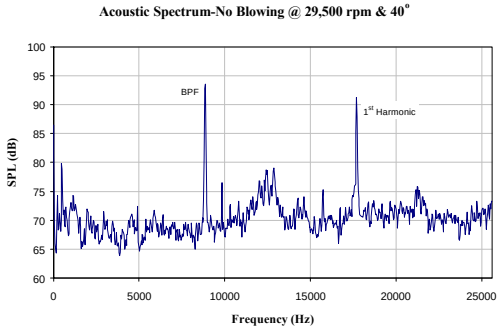

Acoustic Spectrum-No Blowing @ 29,500 rpm & 50°

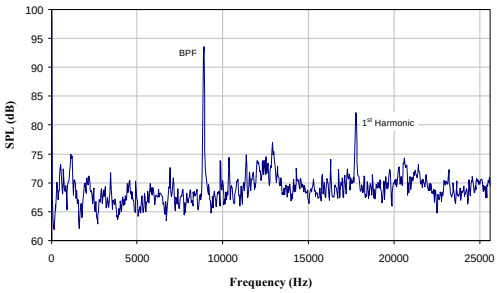

Acoustic Spectrum-No Blowing @ 29,500 rpm & 90°

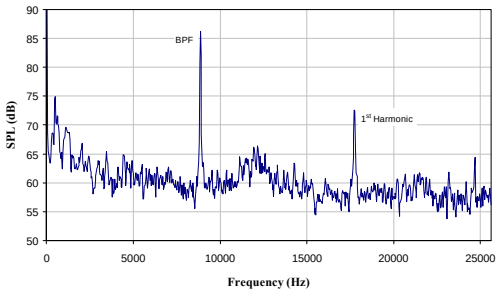

Acoustic Spectrum-No Blowing @ 29,500 rpm & 60°

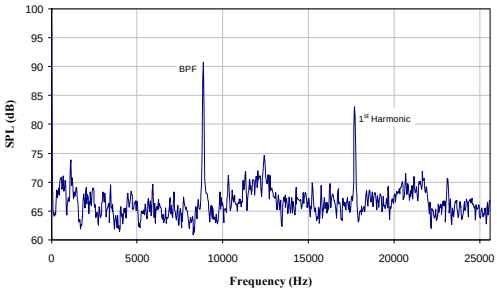

Acoustic Spectrum-No Blowing @ 29,500 rpm & 100°

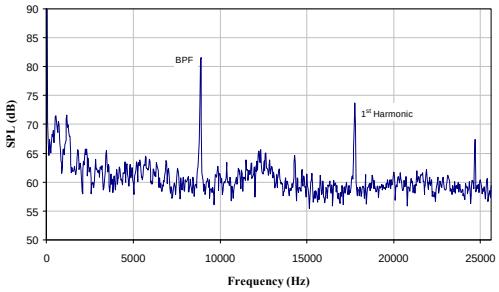

Acoustic Spectrum-No Blowing @ 29,500 rpm & 70°

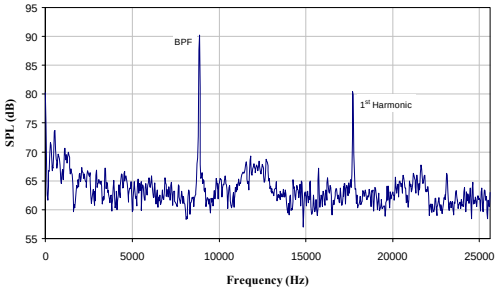

Acoustic Spectrum-No Blowing @ 29,500 rpm & 110°

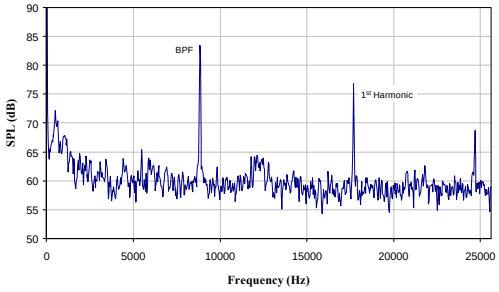

Acoustic Spectrum-No Blowing @ 29,500 rpm & 80°

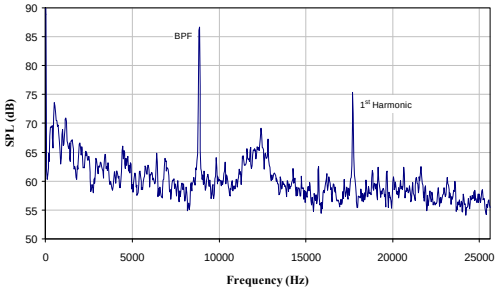

Acoustic Spectrum-With Blowing @ 29,500 rpm & 0°

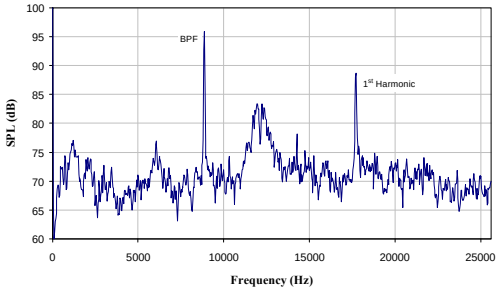

Acoustic Spectrum-With Blowing @ 29,500 rpm & 10°

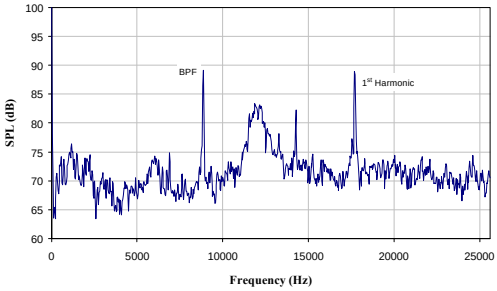

Acoustic Spectrum-With Blowing @ 29,500 rpm & 20°

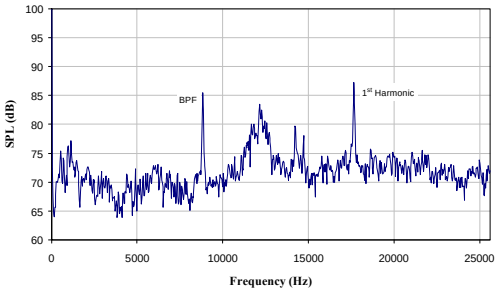

Acoustic Spectrum-With Blowing @ 29,500 rpm & 30°

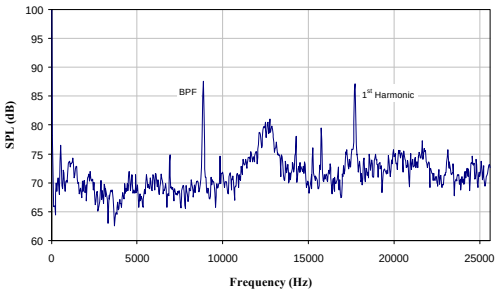

Acoustic Spectrum-With Blowing @ 29,500 rpm & 40°

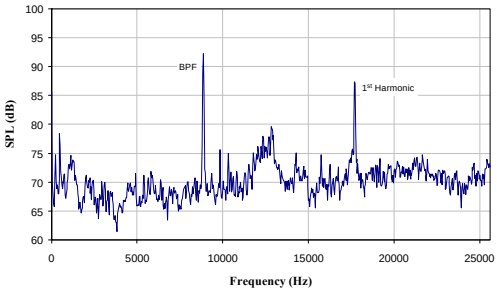

Acoustic Spectrum-With Blowing @ 29,500 rpm & 50°

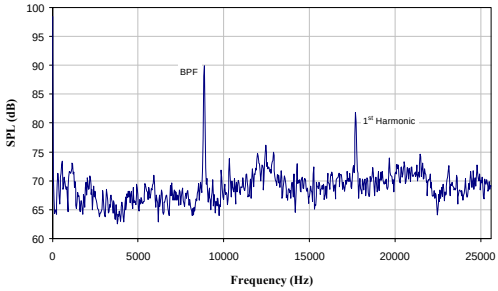

Acoustic Spectrum-With Blowing @ 29,500 rpm & 60°

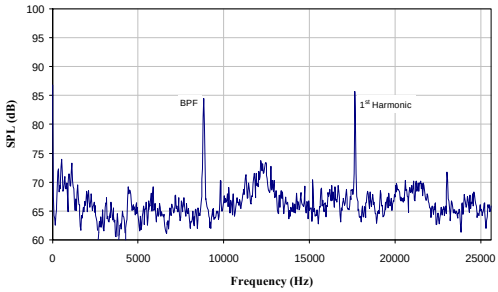

Acoustic Spectrum-With Blowing @ 29,500 rpm & 70°

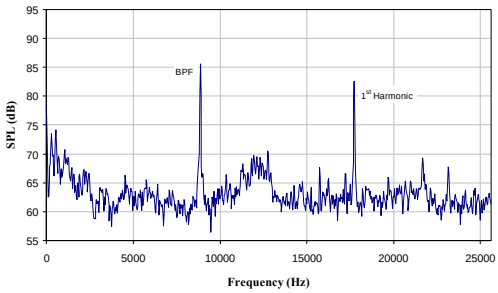

Acoustic Spectrum-With Blowing @ 29,500 rpm & 80°

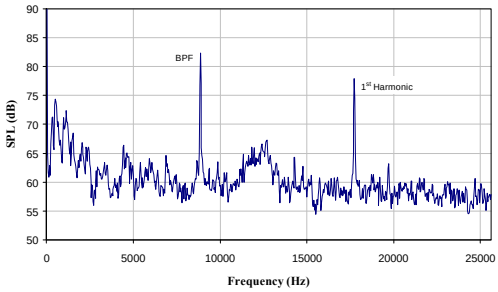

Acoustic Spectrum-With Blowing @ 29,500 rpm & 90°

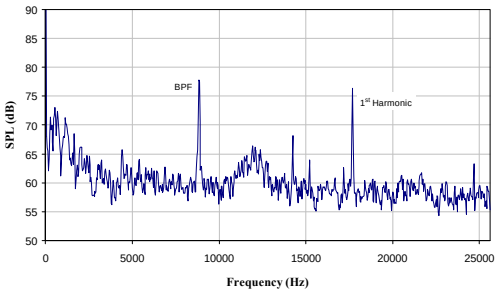

Acoustic Spectrum-No Blowing @ 40,000 rpm & 10°

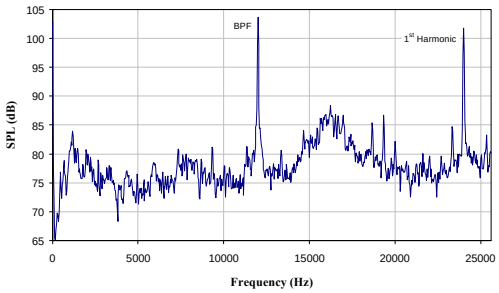

Acoustic Spectrum-With Blowing @ 29,500 rpm & 100°

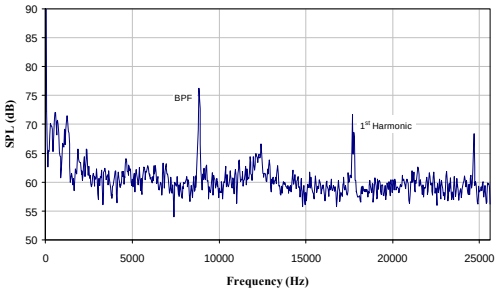

Acoustic Spectrum-No Blowing @ 40,000 rpm & 20°

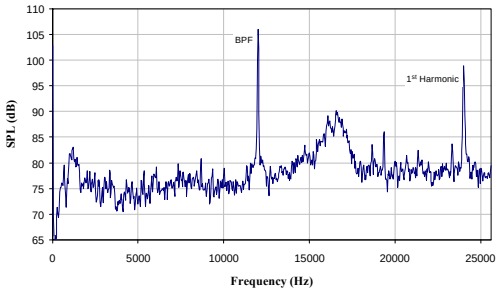

Acoustic Spectrum-With Blowing @ 29,500 rpm & 110°

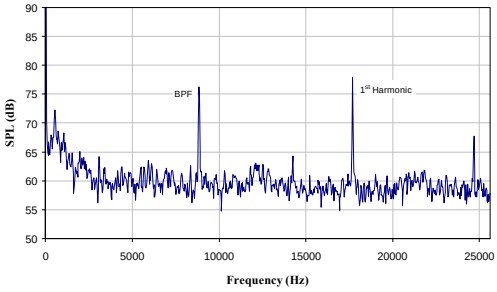

Acoustic Spectrum-No Blowing @ 40,000 rpm & 30°

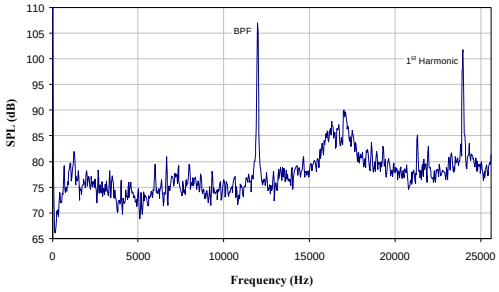

Acoustic Spectrum-No Blowing @ 40,000 rpm & 0°

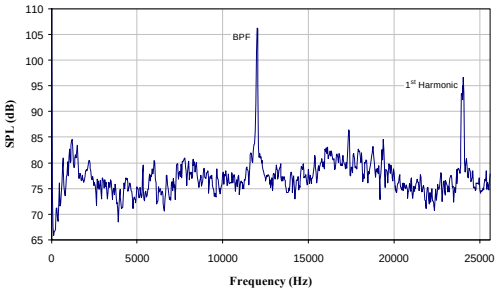

Acoustic Spectrum-No Blowing @ 40,000 rpm & 40°

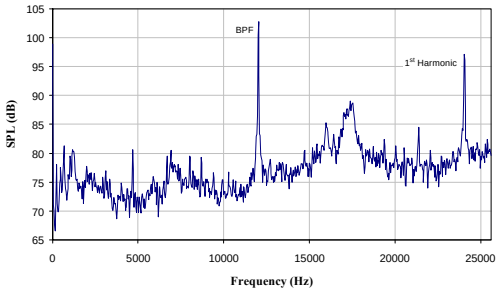

Acoustic Spectrum-With Blowing @ 40,000 rpm & 50°

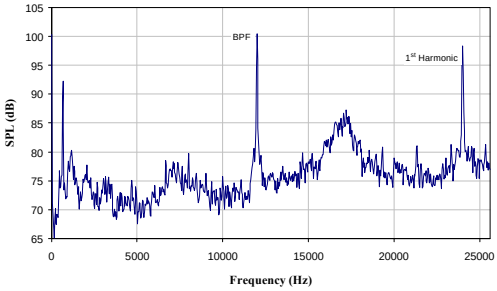

Acoustic Spectrum-No Blowing @ 40,000 rpm & 90°

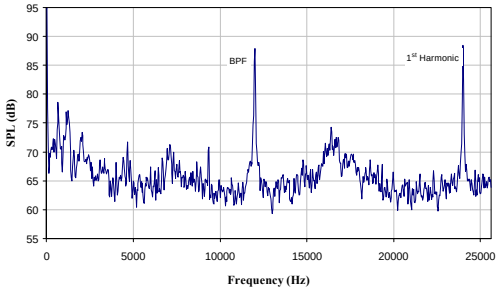

Acoustic Spectrum-No Blowing @ 40,000 rpm & 60°

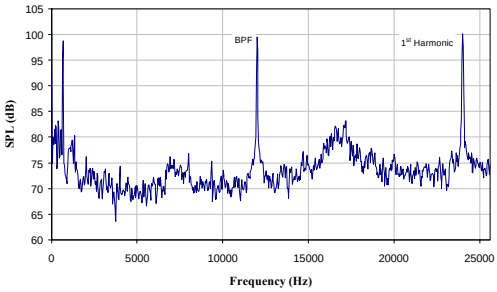

Acoustic Spectrum-No Blowing @40,000 rpm & 100°

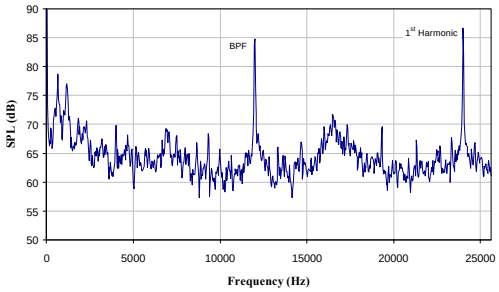

Acoustic Spectrum-No Blowing @ 40,000 rpm & 70°

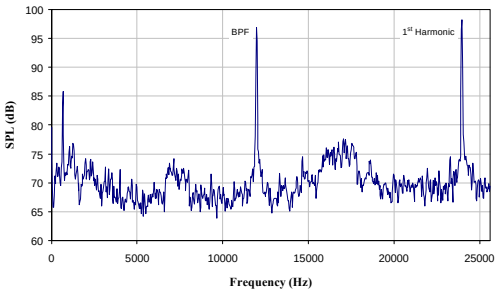

Acoustic Spectrum-No Blowing @ 40,000 rpm & 110°

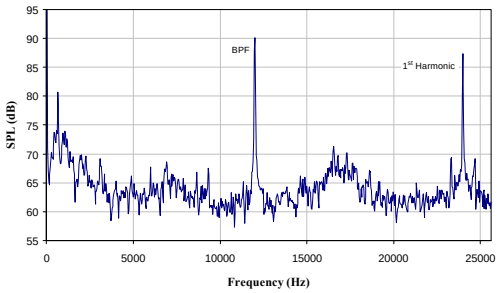

Acoustic Spectrum-No Blowing @ 40,000 rpm & 80°

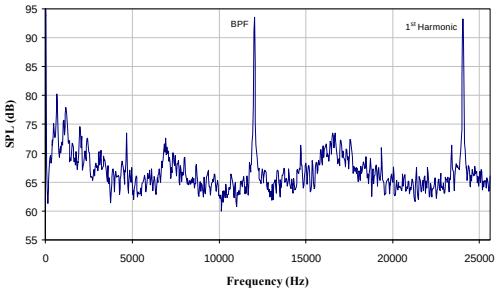

Acoustic Spectrum-With Blowing @ 40,000 rpm & 0°

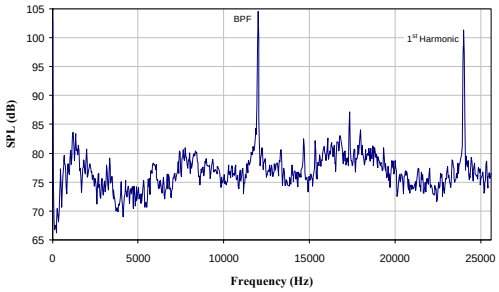

Acoustic Spectrum-With Blowing @ 40,000 rpm & 10°

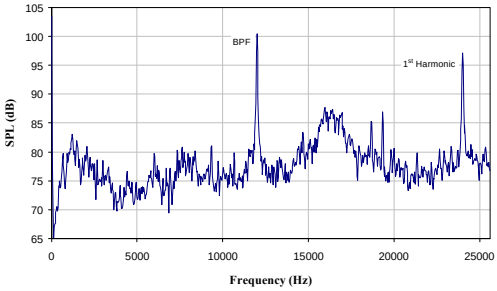

Acoustic Spectrum-With Blowing @ 40,000 rpm & 50°

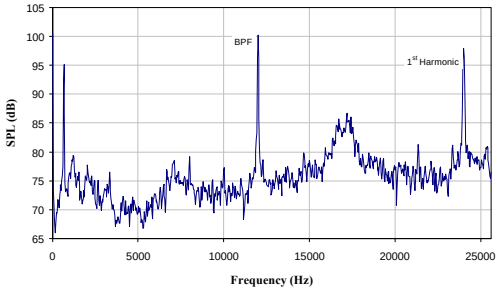

Acoustic Spectrum-With Blowing @ 40,000 rpm & 20°

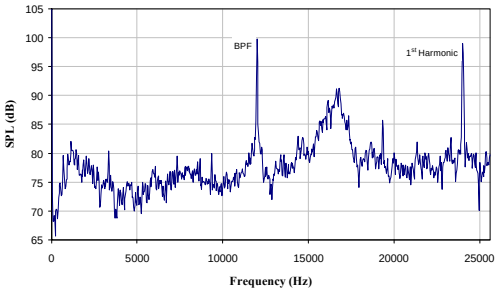

Acoustic Spectrum-With Blowing @ 40,000 rpm & 60°

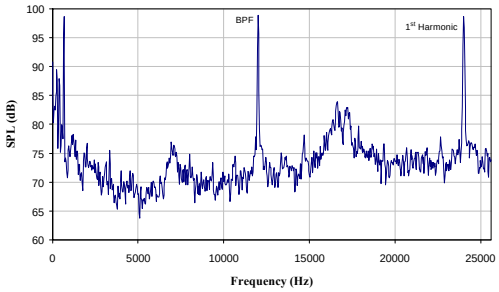

Acoustic Spectrum-With Blowing @ 40,000 rpm & 30°

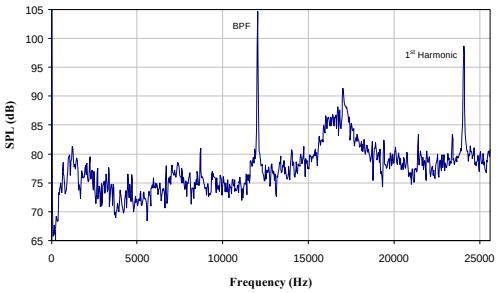

Acoustic Spectrum-With Blowing @ 40,000 rpm & 70°

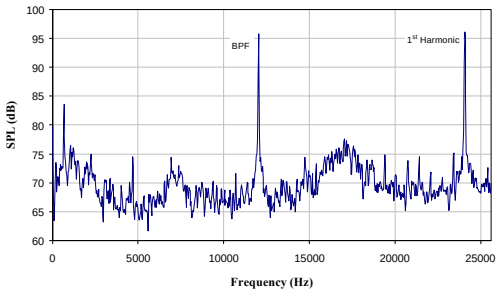

Acoustic Spectrum-With Blowing @ 40,000 rpm & 40°

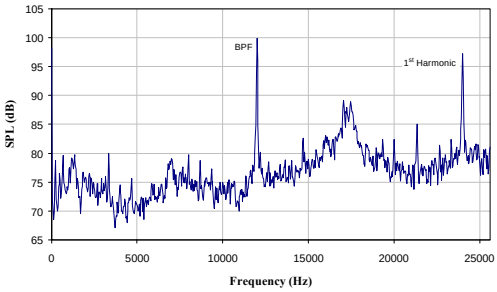

Acoustic Spectrum-With Blowing @ 40,000 rpm & 80°

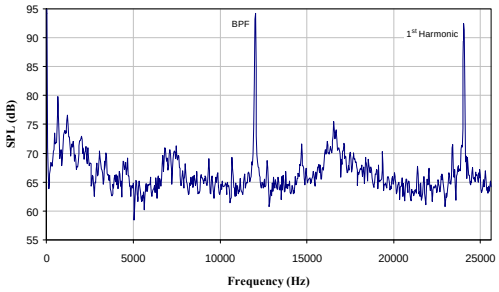

Acoustic Spectrum-With Blowing @ 40,000 rpm & 90°

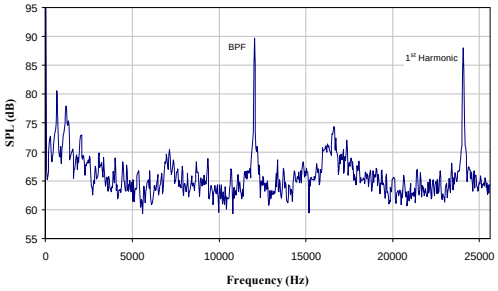

Acoustic Spectrum-With Blowing @40,000 rpm & 100°

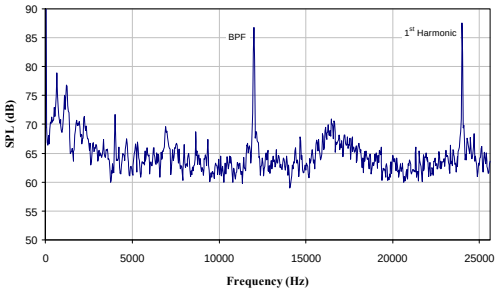

Acoustic Spectrum-With Blowing @ 40,000 rpm & 110°

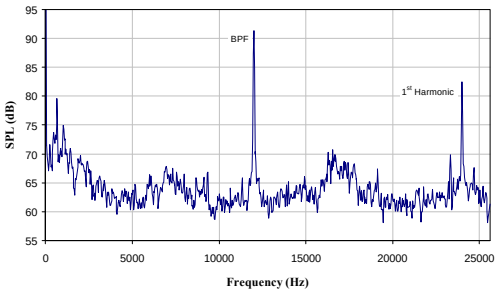

Vita

Nikhil M. Rao was born in Pune, India on July 6 1971. He graduated with Distinction with a Bachelor of Engineering in Mechanical Engineering in August 1993, from the National Institute of Engineering, Mysore University, Mysore. Following his graduation the author gained valuable experience at TurboTech Precision Engineering (P) Ltd., Bangalore, working there from May of 1994 to May of 1997. The author began his graduate studies at Virginia Polytechnic Institute & State Univeristy in May 1997 and commenced his research under Dr. W. F. Ng. Following his graduation in May 1999, the author will pursue his Doctoral research at the Center for Gas Turbine and Power at Pennsylvania State University under Dr. B. Lakshminarayana. The author defended his Masters thesis on April 16 1999.

_____

Nikhil M. Rao